AGU PUBLICATIONS

Journal of Advances in Modeling Earth Systems

RESEARCH ARTICLE

10.1002/2015MS000431

Key Points:
- Large eddy simulation using a general circulation model ICON is presented
- ICON is validated against standard LES models for boundary layer simulations
- Despite limitations, ICON performs well compared to the standard LES models

Correspondence to:
A. Dipankar,
anurag.dipankar@mpimet.mpg.de

Citation:
Dipankar, A., B. Stevens, R. Heinze, C. Moseley, G. Zängl, M. Giorgetta, and S. Brdar (2015), Large eddy simulation using the general circulation model ICON, *J. Adv. Model. Earth Syst.*, *7*, 963–986, doi:10.1002/2015MS000431.

Received 21 JAN 2015
Accepted 2 JUN 2015
Accepted article online 16 JUN 2015
Published online 2 JUL 2015

Large eddy simulation using the general circulation model ICON

Anurag Dipankar[1], Bjorn Stevens[1], Rieke Heinze[2], Christopher Moseley[1], Günther Zängl[3], Marco Giorgetta[1], and Slavko Brdar[3]

[1]Max Planck Institute for Meteorology, Hamburg, Germany, [2]Institute for Meteorology and Climatology, Leibniz University of Hannover, Hannover, Germany, [3]Deutscher Wetterdienst, Offenbach, Germany

Abstract ICON (ICOsahedral Nonhydrostatic) is a unified modeling system for global numerical weather prediction (NWP) and climate studies. Validation of its dynamical core against a test suite for numerical weather forecasting has been recently published by Zängl et al. (2014). In the present work, an extension of ICON is presented that enables it to perform as a large eddy simulation (LES) model. The details of the implementation of the LES turbulence scheme in ICON are explained and test cases are performed to validate it against two standard LES models. Despite the limitations that ICON inherits from being a unified modeling system, it performs well in capturing the mean flow characteristics and the turbulent statistics of two simulated flow configurations—one being a dry convective boundary layer and the other a cumulus-topped planetary boundary layer.

1. Introduction

Understanding climate change requires clear understanding of feedbacks due to clouds, which are the leading source of uncertainty in the existing climate models [*Bony et al*., 2004; *Stevens and Bony*, 2013]. The uncertainty in cloud fields in climate models is in turn due largely to the limitations of the shallow and deep convective parameterization schemes. Different modeling approaches like single column models [*Betts and Miller*, 1986; *Randall et al*., 1996; *Ghan et al*., 2000], cloud resolving modeling [*Xu et al*., 1992; *Xu and Arakawa*, 1992; *Grabowski et al*., 1996], and superparameterization [*Grabowski*, 2001; *Khairoutdinov et al*., 2005] have been used in the past to understand convective parameterization in a climate model.

With the increasing availability of computing resources, efforts have been taken to perform global simulations at even higher resolution to possibly reduce the uncertainty by explicitly resolving some of the scales involved in the convective motion. A good example of this approach is the Japanese model NICAM, which has been used in the recent years to perform global cloud resolving simulations [*Miura et al*., 2007; *Satoh et al*., 2014]. While one can argue about the deep convective scales that are resolved in a typical cloud resolving model with grid resolution ranging from 1 to 4 km, the grid resolution used in such models is definitely too coarse to resolve shallow convection [*Miller*, 1978; *Bryan et al*., 2003]. Moreover, the subgrid turbulence schemes used in the aforementioned cloud resolving models are typically not even designed to work in these resolution ranges. This motivated *Wyngaard* [2004] to refer to this range of scales, where convection is neither resolved nor so unresolved as to be representable in terms of its ensemble effects, as "gray zone."

The only way to avoid this gray zone is by explicitly resolving shallow cumulus convection, which is defined by the depth of the atmospheric boundary layer, which is typically of the order of a kilometer. Thus, simulations on a $\mathcal{O}$(100 m) grid largely obviate the need for special parameterization for organized turbulent motions such as those that define the atmospheric boundary layer and the areas of shallow convection. By crossing this threshold of $\mathcal{O}$(100 m) grid resolution one can begin thinking of LES, wherein the subgrid-scale parameterizations have a sounder theoretical foundation and matter less [*Deardorff*, 1970; *Moeng*, 1984; *Bryan et al*., 2003]. This motivated us to work toward simulations at $\mathcal{O}$(100 m) horizontal resolution, on a sufficiently large domain for sufficiently long time, which will help us to understand the parameterized convection better, and possibly, to improve it.

To take this forward, the German Federal Ministry of Education and Research (BMBF) has initiated a project named High Definition Clouds and Precipitation for advancing Climate Prediction (HD(CP)^2), incorporating

several institutes across Germany. The project targets limited-area LES at resolution $\mathcal{O}$(100 m). There are other groups across the world also moving in this direction of ultra-high resolved simulation in a quasi-operational sense. Some of them, within our knowledge, are *Chow et al*. [2006], *Moeng et al*. [2007], and *Hanley et al*. [2013], who have modified existing regional models to do LES. We use ICON as the host model which is a new nonhydrostatic modeling system, developed in collaboration between the German Weather Service (DWD) and the Max Planck Institute for Meteorology (MPI-M). ICON is different from the models mentioned above because it is a unified modeling system suitable for global and limited-area applications on one hand and for climate prediction and weather forecasting on the other. After the inclusion of LES capabilities, ICON can now be refined to the spatial scales needed to resolve convection while interacting with the evolving large-scale atmosphere.

Admittedly, ICON is not the only unified modeling system known in literature. The Advanced Research WRF (AR-WRF) [*Skamarock et al*., 2008], for example, is a nonhydrostatic fully compressible modeling system which also has capabilities to perform global as well as limited-area simulations with suite of physics packages relevant for climate predictions, NWP, and LES. There is however an important distinction between AR-WRF and ICON in that ICON is an operational global NWP and climate model, which in this manuscript is shown to be flexible enough to be run as a LES model.

The purpose of this paper is to describe the new physics package (LES physics) in the ICON framework and compare its performance against well-established standard LES models for idealized boundary layer flows. We do not present ICON as an alternative to standard LES models that are designed primarily for boundary layer studies. Rather, we aim to utilize the unified nature of ICON by using its eddy-resolving abilities to better understand the processes that are parameterized in the climate or numerical weather forecast configurations of ICON. The model equations and the necessary changes made in ICON to get the new LES physics package are described in the following section. It is important to realize that ICON inherits some compromises from being a unified model that standard LES models do not. For example, while standard LES models use structured orthogonal grids which easily allow to implement higher-accuracy schemes, ICON uses an unstructured icosahedral grid, suitable for spherical geometry, which puts a restriction on the use of a higher-accuracy scheme at a reasonable computational cost. These challenges are apparent in section 3 where the conservative discretization of the three-dimensional turbulence scheme on the ICON grid and its coupling to the model dynamics are explained. The model is then validated against two standard LES models for the following boundary layer flow types: (a) dry convective boundary layer in section 4.1, and (b) cloud topped boundary layer in section 4.2. Concluding remarks are presented in section 5.

2. Model Description

ICON is a fully compressible model that uses geodesic Delaunay grids with C-type staggering, and has the ability to locally refine a region using the classical nesting approach. Much effort has been put in designing the code for high performance on massively parallel computing architectures. The model presently hosts two basic physics packages: one for weather predictions (DWD package) and the second for climate modeling applications (MPI-M package). These two packages are designed for subgrid-scale processes operative on scales of hundreds of kilometers to tens of kilometers. In order to use ICON at $\mathcal{O}$(100 m) scales, a new LES physics package has been added to ICON incorporating the following modifications.

Some of the parameterizations in the DWD and MPI-M packages are invalid at $\mathcal{O}$(100 m) scales and must be turned off. This pertains to the schemes for convection, subgrid-scale orographic effects (blocking and gravity wave drag) and nonorographic gravity wave drag. On the other hand, new approaches for representing the subgrid-scale turbulence and more complex microphysical process must be introduced. Therefore, a new subgrid-scale turbulence scheme based on the classical Smagorinsky scheme has been implemented. The scheme uses the modifications by *Lilly* [1962] to account for thermal stratification. A double-moment microphysics scheme based on *Seifert and Beheng* [2001] has also been implemented for the LES package. Furthermore, instead of the default diagnostic cloud fraction scheme, a simple all-or-nothing scheme [*Sommeria and Deardorff*, 1977] is used that assumes that the cloud fraction within a grid box is either 1 or 0. The default artificial numerical dissipation for LES studies is reduced to fourth order for the momentum equations.

Full details of the set of equations used in ICON and its numerical treatment are beyond the scope of the present work and can be found in *Zängl et al.* [2014] and *Wan et al.* [2013]. Only information relevant to the implementation of the turbulence scheme in ICON are discussed here. Information about the time integration scheme, the spatial discretization schemes, and a few other numerical details are also given in section 4.

The equations employed in ICON are based on the prognostic variables suggested by *Gassmann and Herzog* [2008], and it uses a vector-invariant form for the nonlinear momentum advection terms. The prognostic variables are the horizontal velocity component normal to the triangle edges v_n, the vertical wind component w, density ρ, the density potential temperature θ_ρ [*Stevens*, 2007] (also referred to as virtual potential temperature θ_v [*Zängl et al.*, 2014]), and the specific masses and number densities of tracers q_i (i = 1,2,3. . .,N_t). The tracers include water vapor (q_v), liquid water (q_l), snow (q_s), ice (q_i), etc. N_t is the total number of tracers which depends on the microphysics scheme used. Here ρ is the full air density including liquid and solid condensates, and

$$\theta_\rho = T_\rho \left(\frac{p_{00}}{p} \right)^{R_d/c_{pd}} = \frac{T_\rho}{\pi} . \tag{1}$$

In the above equation, p_{00} is the reference pressure, π is the Exner function, and $T_\rho = T\alpha$ is the density temperature with

$$\alpha = [1 + (R_v/R_d - 1)q_v - q_c], \tag{2}$$

where $q_c = \Sigma_{i \in \text{hydrometeors}}\, q_i$ is the contribution due to liquid and solid condensates, R_d and R_v are the gas constants for dry air and water vapor, respectively, and c_{pd} is the isobaric specific heat capacity of dry air.

The turbulent fields in the model are filtered as

$$\phi = \tilde{\phi} + \phi' , \tag{3}$$

where $\tilde{\phi}$ is Favre-filtered [*Hinze*, 1975]

$$\tilde{\phi} = \frac{\overline{\rho\phi}}{\bar{\rho}} . \tag{4}$$

The *overbar* $\overline{()}$ indicates the filtering in the traditional manner as used in incompressible flows [*Sagaut*, 1998, p. 16]. For better readability, we henceforth use x_i and v_i to indicate the three ($i \in (1, 2, 3)$) orthogonal axes and the respective velocity components. Here x_1 denotes the horizontal axis normal to the triangle edge and x_2 denotes the horizontal axis parallel to the triangle edge (see unit vectors 1, 2 in Figure 1). The vertical coordinate is denoted by x_3, which points in the upward direction as indicated by $\odot$ in Figure 1. The velocity vector (v_1,v_2,v_3) forms a right-handed system. Following this convention, the Navier-Stokes equations used in the model can be written as:

$$\frac{\partial \widetilde{v_1}}{\partial t} + \frac{\partial (\widetilde{\mathbf{v_h}} . \widetilde{\mathbf{v_h}}/2)}{\partial x_1} - (\zeta + f)\widetilde{v_2} + \widetilde{v_3}\frac{\partial \widetilde{v_1}}{\partial x_3} = -c_{pd}\widetilde{\theta_\rho}\frac{\partial \bar{\pi}}{\partial x_1} + Q_{v_1} , \tag{5}$$

$$\frac{\partial \widetilde{v_3}}{\partial t} + \widetilde{\mathbf{v_h}} . \nabla_{\mathbf{h}} \widetilde{v_3} + \widetilde{v_3}\frac{\partial \widetilde{v_3}}{\partial x_3} = -c_{pd}\widetilde{\theta_\rho}\frac{\partial \bar{\pi}}{\partial x_3} - g + Q_{v_3} , \tag{6}$$

$$\frac{\partial \bar{\rho}}{\partial t} + \nabla . (\tilde{\mathbf{v}}\bar{\rho}) = 0 , \tag{7}$$

where, $\mathbf{v_h}$ and $\mathbf{v}$ are the horizontal and full three-dimensional (3-D) velocity components, respectively, ζ is the vertical vorticity component, f is the Coriolis parameter. It is to be noted that the model only solves for v_1, and the tangential velocity component (v_2) is diagnosed using the radial basis function (RBF) reconstruction [*Narcovich and Ward*, 1994].

The turbulent parameterization terms, Q_{v_k}, are calculated as the divergence of the subgrid-scale stress tensor τ_{kl}

$$Q_{v_k} = \left(\frac{\partial \tilde{v}_k}{\partial t} \right)_{\text{turb}} = \frac{1}{\bar{\rho}}\frac{\partial \tau_{kl}}{\partial x_l} . \tag{8}$$

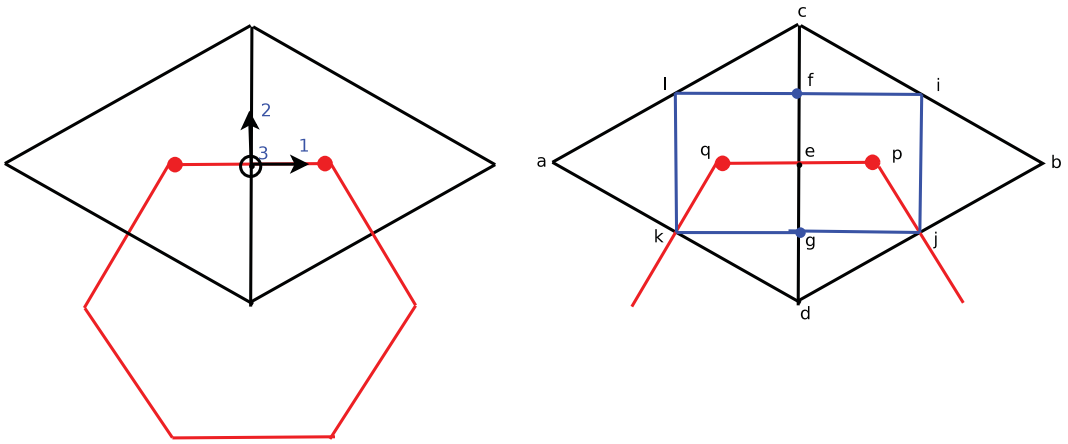

Figure 1. (left) Schematic showing the primal (black triangles) and dual (red hexagons) cells, and the associated local coordinate system used in this manuscript. Unit vectors 1, 2, and 3 point in the direction of edge normal, tangent, and vertically upward (indicated by ⊙), respectively. (right) Schematic of two adjacent triangles in ICON grid identifying the various locations used to discretize the turbulent diffusion term. *a*, *b*, *c*, *d* are the triangle vertices, *e* is the center of the edge *cd* about which all the strain rates are calculated, and *p*, *q* are the cell-centers.

Herein, the Einstein summation convention applies to repeated indices. The subgrid-scale stress tensor is then parameterized following *Lilly* [1962] as

$$\tau_{kl} = K_m \left(\tilde{S}_{kl} - \frac{1}{3} \tilde{S}_{mm} \delta_{kl} \right), \tag{9}$$

where K_m is the subgrid viscosity

$$K_m = 2\lambda^2 \tilde{\rho} |S| \left(1 - \frac{\mathrm{Ri}}{\mathrm{Pr}_t} \right)^{1/2} \quad \text{for } 1 - \frac{\mathrm{Ri}}{\mathrm{Pr}_t} > 0. \tag{10}$$

Here λ is the subgrid length scale proportional to the grid volume, $\Delta = (\Delta_1 \Delta_2 \Delta_3)^{1/3}$, and the Smagorinsky constant C_s. It is varied in vertical following *Mason and Brown* [1999] as

$$\frac{1}{\lambda^2} = \frac{1}{(C_s \Delta)^2} + \frac{1}{(\kappa x_3)^2}. \tag{11}$$

In the case that the grid is vertically stretched, the maximum grid volume in the first model level near the surface is used for Δ. The other terms in equations (9–11) are the von Karman constant κ, the turbulent Prandtl number Pr_t, and $|S| = (\tilde{S}_{mn} \tilde{S}_{mn})^{1/2}$ where $\tilde{S}_{kl}$ is the Favre-filtered rate of strain tensor given by

$$\tilde{S}_{kl} = \frac{1}{2} \left(\frac{\partial \tilde{v}_k}{\partial x_l} + \frac{\partial \tilde{v}_l}{\partial x_k} \right). \tag{12}$$

The Richardson number, Ri, in equation (10) is calculated as

$$\mathrm{Ri} = \begin{cases} \dfrac{N_m^2}{|S|^2} & \text{for saturated air} \\ \dfrac{N^2}{|S|^2} & \text{for unsaturated air,} \end{cases} \tag{13}$$

where N and N_m are the dry and the moist Brunt Väisälä frequency defined, following *Durran and Klemp* [1982], as

$$\begin{aligned} N^2 &= \frac{g}{\theta} \frac{\partial \theta}{\partial x_3}, \\ N_m^2 &= \left[N^2 + \frac{g}{T} (\Gamma_m - \Gamma_d) \right] \left(1 + \frac{L_v q_{sat}}{R_d T} \right). \end{aligned} \tag{14}$$

Here Γ_d and Γ_m are the dry and the moist adiabatic lapse rate, respectively, L_v is the latent heat of vaporization, and θ is the potential temperature.

The thermodynamic equation expressed in terms of the density potential temperature and the budget equations for the tracers in ICON are expressed as

$$\frac{\partial \bar{\rho}\tilde{\theta}_\rho}{\partial t} + \nabla.(\tilde{\mathbf{v}}\bar{\rho}\tilde{\theta}_\rho) = Q_{\theta_\rho}\,, \tag{15}$$

$$\frac{\partial \bar{\rho}\tilde{q}_i}{\partial t} + \nabla.(\tilde{\mathbf{v}}\bar{\rho}\tilde{q}_i) = Q_{q_i}\,. \tag{16}$$

Here Q_{θ_ρ} and Q_{q_i} represent the forcing from the slow-physics (i.e., radiation) and the fast-physics parameterizations (i.e., saturation adjustment, cloud microphysics, and turbulence). Note that Q_{v_1} and Q_{v_2} in equations (5–7) are also categorized as fast-physics. As the name suggests, the slow-physics are called less frequently compared to the fast-physics and therefore their tendencies are stored to be integrated with the governing equation. The fast-physics, on the other hand, are called every physics time step to sequentially update the prognostic variables and therefore do not provide tendencies to the governing equations. The sequential coupling between the turbulence parameterization and the dynamics is explained in Appendix A.

Equations (5–7) and equation (15), together with the slow-physics tendencies, are integrated in time using the two-time level predictor-corrector scheme except for the terms corresponding to the vertical sound-wave propagation, which are integrated implicitly. Tracers in equation (16) are integrated using a flux-form semi-Lagrangian scheme for its better conservation properties. As rather small time steps are required for the dynamics to maintain numerical stability, it is substepped several times between successive calls to the physical parameterizations. In the default configuration, physics time step is 5 times larger than the dynamics time step.

Radiation and the cloud microphysics have been turned off because of the idealized nature of the test cases. Therefore, Q_{θ_ρ} and Q_{q_i} (for $q_i \in (q_v, q_l)$) only represent the effects of subgrid turbulent diffusion and condensation. That is,

$$Q_{\theta_\rho} = \left(\frac{\partial \tilde{\theta}_\rho}{\partial t}\right)_{\text{turb}} + \left(\frac{\partial \tilde{\theta}_\rho}{\partial t}\right)_{\text{cond}}$$

$$Q_{q_i} = \left(\frac{\partial \tilde{q}_i}{\partial t}\right)_{\text{turb}} + \left(\frac{\partial \tilde{q}_i}{\partial t}\right)_{\text{cond}}.$$

Effects of condensation are calculated using the standard saturation adjustment scheme that assumes a uniform distribution of temperature and humidity within a grid box [*Sommeria*, 1976]. Using equations (1) and (2), the subgrid turbulent term can be expressed in terms of the prognostic variables as

$$\left(\frac{\partial \tilde{\theta}_\rho}{\partial t}\right)_{\text{turb}} = \tilde{\alpha}\left(\frac{\partial \tilde{\theta}}{\partial t}\right)_{\text{turb}} + \tilde{\theta}\left[(R_d/R_v - 1)\left(\frac{\partial \tilde{q}_v}{\partial t}\right)_{\text{turb}} - \left(\frac{\partial \tilde{q}_l}{\partial t}\right)_{\text{turb}}\right],$$

$$\left(\frac{\partial \tilde{q}_i}{\partial t}\right)_{\text{turb}} = \frac{\partial}{\partial x_k}\left(K_h \frac{\partial \tilde{q}_i}{\partial x_k}\right),$$

where

$$\left(\frac{\partial \tilde{\theta}}{\partial t}\right)_{\text{turb}} = \frac{\partial}{\partial x_k}\left(K_h \frac{\partial \tilde{\theta}}{\partial x_k}\right). \tag{17}$$

Here $K_h = \frac{K_m}{\text{Pr}_t}$ is the eddy diffusivity coefficient, which is assumed to be same for $\tilde{\theta}$ and $\tilde{q}_i$. Pr_t is set to 1/3.

We note that the governing equations in ICON differ from standard LES models in many ways. For example, in ICON only one of the horizontal velocity components (v_1) is prognosed while the other component (v_2) is diagnosed, and both the thermodynamic and the tracer equations use nonconservative variables. Standard LES models, on the other hand, typically prognose both the horizontal velocity components and use

conserved (in nonprecipitating convective motions [*Deardorff*, 1980]) thermodynamic variables like liquid water potential temperature (θ_l) and total liquid water (q_t). These differences are discussed in more detail in section 4 when the other two LES models are introduced.

3. Numerical Implementation

In the following, we discuss in detail the implementation of the subgrid-scale turbulence term on the ICON grid. Details on the coupling between the dynamics and the turbulence parameterization, and the time integration of the turbulent diffusion terms are given in Appendix A. Note that the use of *tilde* $\widetilde{()}$ and *overbar* $\overline{()}$ on filtered variables are dropped henceforth for notational simplicity. The implementation of the diffusion terms presented here assumes a flat surface that is suitable for the idealized runs discussed in this paper. The full formulation over nonflat surfaces will be discussed in a subsequent work.

The local coordinate system used for the discretization is indicated in Figure 1 by the unit vectors 1, 2, and 3. The (right) schematic shows two triangles, *adc* and *dbc* with common edge *cd*, where *e* is the center of the local axes. The (circum-) centers of the triangles are indicated by *p* and *q*. We follow the C-gridtype arrangement of *Arakawa* [1966]: v_1 is located at the edge-center *e* of the full (main) vertical levels; v_2 is located at the center of the dual-edge *pq* of the full levels, as indicated by the red line(s) in the figure, which by design coincides with *e*; v_3 is located at the cell-center *p* of the half (interface) vertical levels; and temperature, density, and tracers are stored at the cell-centers of the full vertical levels. The cell-centers are also referred to as mass points in the text.

The various interpolation operators, for an arbitrary variable ϕ, used in this section are:

1. $\bar{\phi}^{ev}$: a RBF reconstruction from edges to vertices.
2. $\bar{\phi}^{e}$: a linear interpolation from mass points or vertices to edges.
3. $\bar{\phi}^{c}$: a bilinear interpolation from edges to mass points.
4. $\bar{\phi}^{cv}$: an area-weighted interpolation from mass points to vertices.
5. $\bar{\phi}^{i}$: a linear interpolation from main levels to interface levels (quadratic extrapolation at the surface).
6. $\bar{\phi}^{m}$: a linear interpolation from interface levels to main levels.

The letters next to the *overbar* $\overline{()}$ here indicate the location to which the interpolation is performed, except for $\bar{\phi}^{ev}$ and $\bar{\phi}^{cv}$, which indicate interpolation from edge-to-vertices and cells (mass points)-to-vertices, respectively. RBF reconstruction in ICON uses the Gaussian basis function, $e^{-(r/\beta)^2}$, with shape parameter, β, tuned for great circle distances *r* [*Wan et al*., 2013]. For the flat surfaces, the basis function uses the Cartesian distance as *r*, which requires changing β for better performance. For now, it has been set to twice the length of the dual-edge (*pq*), which gives reasonable accuracy but further investigation is required.

The discrete operators used in this section are

$$\Delta_{mn}\phi = \phi_n - \phi_m, \tag{18}$$

$$\Delta_{x_3}\phi(x_1, x_2, x_3) = \phi(x_1, x_2, x_3 + h) - \phi(x_1, x_2, x_3 - h), \tag{19}$$

where $h = \frac{\Delta x_3}{2}$ is half of the vertical spacing at a given level. In the following, it will become clear that these difference operators are intended for implementing a second-order central difference scheme. For spherical triangles, however, the horizontal differences in the edge-normal direction may not be truly centered, especially when the triangles become distorted by the nonuniform tiling of the sphere. Errors because of this are generally small, and they decrease as the resolution increases, but such distortion limits the order of the discrete operators. For the idealized test cases presented in this paper, these difference operators are truly centered because the mesh is on a plane with equilateral triangles.

3.1. Subgrid Viscosity

Different strategies are used to calculate strain rates for the subgrid viscosity (K_m) and for the turbulent fluxes. While they are estimated at their natural locations for the turbulent fluxes (shown in section 3.2), for K_m they are all estimated at the edge-center (e.g., *e* in Figure 1) of the full levels for coding convenience.

$$S_{11}=\frac{\partial v_1}{\partial x_1}=\frac{\Delta_{ab}\overline{v_1}^{ev}}{\Delta_{ab}x_1}, \tag{20}$$

$$S_{12}=\frac{1}{2}\left(\frac{\partial v_1}{\partial x_2}+\frac{\partial v_2}{\partial x_1}\right)=\frac{1}{2}\left(\frac{\Delta_{dc}\overline{v_1}^{ev}}{\Delta_{dc}x_2}+\frac{\Delta_{ab}\overline{v_2}^{ev}}{\Delta_{ab}x_1}\right), \tag{21}$$

$$S_{13}=\frac{1}{2}\left(\frac{\partial v_1}{\partial x_3}+\frac{\partial v_3}{\partial x_1}\right)=\frac{1}{2}\left(\frac{\Delta_{x_3}\overline{v_1}^{i}}{\Delta x_3}+\frac{\Delta_{qp}\overline{v_3}^{m}}{\Delta_{qp}x_1}\right), \tag{22}$$

$$S_{21}=S_{12}, \tag{23}$$

$$S_{22}=\frac{\partial v_2}{\partial x_2}=\frac{\Delta_{dc}\overline{v_2}^{ev}}{\Delta_{dc}x_2}, \tag{24}$$

$$S_{23}=\frac{1}{2}\left(\frac{\partial v_2}{\partial x_3}+\frac{\partial v_3}{\partial x_2}\right)=\frac{1}{2}\left(\frac{\Delta_{x_3}\overline{v_2}^{i}}{\Delta x_3}+\frac{\Delta_{dc}\overline{\overline{v_3}^{cv}}^{m}}{\Delta_{dc}x_2}\right), \tag{25}$$

$$S_{31}=S_{13}, \tag{26}$$

$$S_{32}=S_{23}, \tag{27}$$

$$S_{33}=\frac{\partial v_3}{\partial x_3}=\frac{\Delta_{x_3}\overline{v_3}^{e}}{\Delta x_3}. \tag{28}$$

The above set of equations give strain rates and subgrid viscosity at the edge-center on the full levels. Therefore, interpolation is required to calculate K_m and K_h at the interface levels for the diffusion of v_1, θ, and all the tracers. The effectiveness of the diffusive transport is found to be very sensitive to this interpolation [*Stevens et al.*, 1999]. Some advocate the use of geometric interpolation over arithmetic interpolation [*Patankar*, 1980, p. 197], but the observations by *Stevens et al.* [1999] suggest otherwise. We also performed simulations to investigate the effect of arithmetic interpolation over geometric interpolation, and found that the latter reduces the value of K_m significantly, making the model unstable. In order to further understand this sensitivity, we also calculated K_m at the half level cell-centers by first interpolating $|S|$ from edges-to the cell- centers and then vertically to the half levels, which is normally done in LES models based on regular grids. The results obtained from both these approaches for the case in section 4.2 were almost indistinguishable from each other (not shown).

3.2. Turbulent Fluxes

The location of the stress terms τ_{1l} and τ_{3l} (same as that of S_{1l} and S_{3l}) used in the calculation of turbulent fluxes are shown in Figure 2, which shows one of the triangles (*acda*) in Figure 1. It is advised to follow both Figures 1 and 2 to understand the discretization explained below. Also, note that the location of a variable, if required, is indicated by $|_{()}$ which should not be confused by the letters used as superscript indicating interpolation scheme. Detailed derivation of some of the turbulent fluxes is given in Appendix B for reference.

The subgrid diffusion term in equation (5) is calculated at the edge-center by discretizing the right-hand side (RHS) of equation (8)

$$\left.\frac{1}{\bar{\rho}^e}\frac{\partial \tau_{1l}}{\partial x_l}\right|_e=\left.\frac{1}{\bar{\rho}^e}\left(\frac{\partial \tau_{11}}{\partial x_1}+\frac{\partial \tau_{12}}{\partial x_2}+\frac{\partial \tau_{13}}{\partial x_3}\right)\right|_e, \tag{29}$$

in flux-form as (see Appendix B for detailed derivation)

$$\left.\frac{1}{\bar{\rho}^e}\frac{\partial \tau_{1l}}{\partial x_l}\right|_e=\frac{1}{\bar{\rho}^e}\left[\frac{\overline{K_m}^{c}|_p\left(\frac{\overline{v_1}^{ev}|_b-v_1|_e}{\Delta_{eb}x_1}-\bar{D}^{c}|_p\right)-\overline{K_m}^{c}|_q\left(\frac{v_1|_e-\overline{v_1}^{ev}|_a}{\Delta_{ae}x_1}-\bar{D}^{c}|_q\right)}{\Delta_{qp}x_1}\right.$$
$$\left.+\frac{\overline{K_m}^{cv}|_c\left(\frac{\overline{v_1}^{ev}|_c-v_1|_e}{\Delta_{ec}x_2}+\frac{\Delta_{ab}\overline{v_2}^{ev}}{\Delta_{ab}x_1}\right)-\overline{K_m}^{cv}|_d\left(\frac{v_1|_e-\overline{v_1}^{ev}|_d}{\Delta_{de}x_2}+\frac{\Delta_{ab}\overline{v_2}^{ev}}{\Delta_{ab}x_1}\right)}{2\Delta_{gf}x_2}+\frac{\Delta_{x_3}\overline{K}_m^{i}\left(\frac{\Delta_{x_3}v_1}{\Delta x_3}+\frac{\Delta_{qp}v_3}{\Delta_{qp}x_1}\right)}{2\Delta x_3}\right]. \tag{30}$$

Here $D=\frac{1}{3}S_{mm}$ that appears in equation (9), which is essentially one-third of the total divergence. All the terms on the RHS of the above equation are integrated in time using Euler explicit except for the term

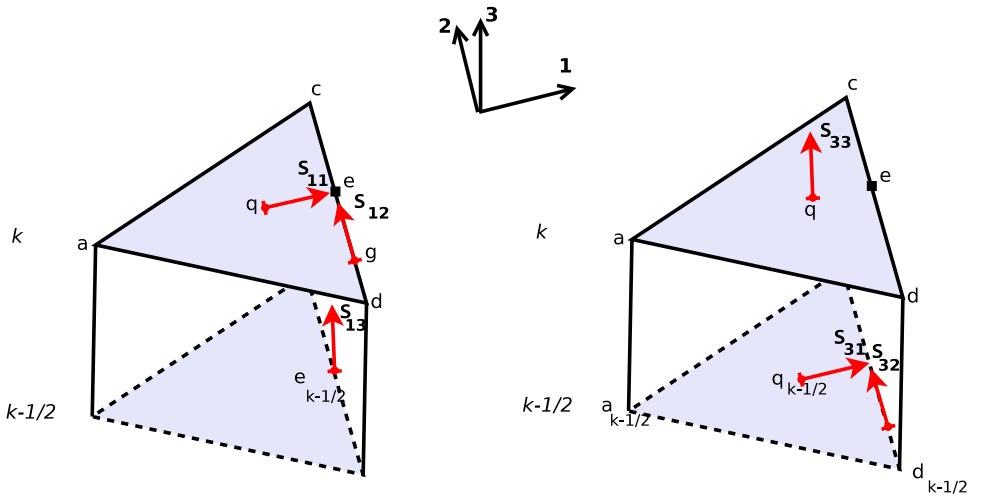

Figure 2. Schematic showing the locations at which the strain rates S_{ij} are defined for (left) horizontal and (right) vertical turbulent diffusion. The full and half vertical levels are indicated by k and $k-1/2$, respectively, and the triangles at the half levels are marked by dashed line. Naming convention same as that of Figure 1 is used. The direction vectors are also indicated in the middle.

$\frac{\Delta_{x_3} v_1}{\Delta x_3}$ contributing to the vertical diffusion, which is integrated using Euler implicit (see Appendix A for details).

The subgrid turbulence term for equation (6) can also be written in a similar manner at the v_3 point as (written without the density term)

$$\left.\frac{\partial \tau_{3l}}{\partial x_l}\right|_{q_{k-1/2}} = \overline{\left.\frac{\partial \tau_{31}}{\partial x_1}\right|_{e_{k-1/2}}}^{c} + \overline{\left.\frac{\partial \tau_{32}}{\partial x_2}\right|_{e_{k-1/2}}}^{c} + \left.\frac{\partial \tau_{33}}{\partial x_3}\right|_{q_{k-1/2}}. \tag{31}$$

It is important to note that the terms $\frac{\partial \tau_{31}}{\partial x_1}$ and $\frac{\partial \tau_{32}}{\partial x_2}$ are first calculated at edge-center of the half levels (see Figure 2) and then interpolated to the cell-center as indicated by $\overline{()}^{c}$ in the equation above. Fully discrete set of equation reads as (dropping out $_{k-1/2}$ for clarity)

$$\left.\frac{\partial \tau_{3l}}{\partial x_l}\right|_q = \frac{\overline{\overline{K_m}^{v^i}|_p \left(\frac{\overline{v_3}^{v}|_b - \overline{v_3}^{e}|_e}{\Delta_{eb} x_1} + \frac{\Delta_{x_3} v_1}{\Delta x_3}|_p\right) - \overline{\overline{K_m}^{v^i}|_q \left(\frac{\overline{v_3}^{v}|_e - \overline{v_3}^{v}|_a}{\Delta_{ea} x_1} + \frac{\Delta_{x_3} v_1}{\Delta x_3}|_q\right)}^{c}}{2\Delta_{qp} x_1}$$

$$+ \frac{\overline{\overline{K_m}^{v^i}|_c \left(\frac{\overline{v_3}^{v}|_c - \overline{v_3}^{e}|_e}{\Delta_{ec} x_2} + \frac{\Delta_{x_3}}{\Delta x_3}\frac{v_2 + \overline{v_2}^{cv}|_c}{2}\right) - \overline{\overline{K_m}^{v^i}|_d \left(\frac{\overline{v_3}^{v}|_d - \overline{v_3}^{e}|_e}{\Delta_{ed} x_2} + \frac{\Delta_{x_3}}{\Delta x_3}\frac{v_2 + \overline{v_2}^{cv}|_d}{2}\right)}^{c}}{2\Delta_{gf} x_2}$$

$$+ \frac{\Delta_{x_3} \overline{K_m}^{c}\left(\frac{\Delta_{x_3} v_3}{\Delta x_3} - \frac{\overline{Div.}^{c}}{3}\right)}{\Delta x_3}. \tag{}$$

Once again, all the terms on the RHS of equation (31) are integrated in time using Euler explicit except for the term $\frac{\partial \tau_{33}}{\partial x_3}$, which is integrated using Euler implicit. The discretization for the turbulent diffusion of cell-centered variables (θ and q_i) is straightforward. The formulation presented below is for equation (17) but the same is applicable for tracers as well,

$$\left(\frac{\partial \tilde{\theta}}{\partial t}\right)_{\text{turb}} = \frac{1}{a_c}\sum K_h \frac{\Delta_{qp}\theta}{\Delta_{qp} x_1} \Delta_{cd} x_1 f_o + \frac{\Delta_{x_3}\left(\overline{K_h}^{i}\frac{\Delta_{x_3}\theta}{\Delta x_3}\right)}{\Delta x_3}. \tag{32}$$

Here a_c is the area of the triangle, f_o is the orientation factor (± 1) indicating the orientation of the triangle edge [*Wan et al.*, 2013]. The first term on the RHS of equation (32) is the horizontal diffusion which is obtained using the divergence theorem by summing the fluxes across the three edges of the triangle.

Similar to the momentum equations, the first term on the RHS of equation (32) is integrated explicitly in time whereas the second term is integrated implicitly.

It is clear that the discretization of the turbulent diffusion terms is flux-conservative. Meeting this conservation requirement on a triangular grid, while maintaining the overall computational performance, is not trivial. This is primarily because of the several interpolations involved which are computationally expensive, and result in loss of accuracy, and depending on the type of interpolation function, smoothening of the interpolant. For some asymptotic descriptions this effectively implies an A-grid implementation [*Gassmann and Herzog*, 2008]. Despite this overhead, the preliminary study revealed that the turbulence scheme in ICON takes about 20% of the overall computational time, which is comparable to the performance of the similar turbulence scheme implemented in a structured grid in one of the standard LES model (UCLA-LES) used here.

3.3. Surface Boundary Condition

Surface fluxes in ICON are parameterized by the drag-law formulation. Surface fluxes of sensible and latent heat in that formulation are written as:

$$(\overline{w'\theta'})_s = -\rho C|\mathbf{v_h}(\Delta x_3)|[\theta(\Delta x_3)-\theta_s], \tag{33}$$

$$(\overline{w'q_v'})_s = -\rho C|\mathbf{v_h}(\Delta x_3)|[q_v(\Delta x_3)-q_{vs}], \tag{34}$$

where the subscript s indicate the value at the surface, C is the bulk-aerodynamical transfer coefficient for turbulent heat exchange at the surface parameterized in ICON following *Louis* [1979], and $\mathbf{v_h}(\Delta x_3)$ is the horizontal velocity at the first model level. Surface temperature, θ_s, is required in equation (33) which is either prescribed, for example, for the idealized simulations, or prognosed by the land-surface model.

Since the subgrid viscosity is calculated at the full levels in the present formulation, Brunt Väisälä frequency (N and N_m) is needed to be calculated at the first model level, which in turn requires θ_s. For the idealized simulations, if not prescribed, it is obtained using the integrated form of the flux-profile relationships [*Louis*, 1979] that assumes logarithmic profile for mean quantities

$$\theta_s = \theta(\Delta x_3) - R\frac{\theta_*}{\kappa}[\ln(\Delta x_3/z_0) - \psi_h(\Delta x_3/L) + \psi_h(z_0/L)], \tag{35}$$

where the constant R (=0.74) is the ratio of the drag coefficients for momentum and heat in the neutral limit, z_0 is the roughness length for momentum, θ_* is the surface layer temperature scale

$$\theta_* = -\frac{(\overline{w'\theta'})_s}{u_*}, \tag{36}$$

and L is the Monin-Obukhov-scale height

$$L = \frac{\theta u_*^2}{\kappa g \theta_*}, \tag{37}$$

where κ is the von Kárman constant, and u_* is the friction velocity. The functions ψ have the same form as in *Louis* [1979] and are therefore not reproduced here.

3.4. Lateral Boundary Condition

Doubly periodic boundary conditions are required for the simulations performed in the present work. This is achieved by treating the grid as a pseudo 2-D torus so that the boundaries in the respective coordinate directions are joined to each other. In order to incorporate this geometry in ICON, modifications have been made in the calculation of the interpolation coefficients and the discrete operators so that it uses Cartesian coordinates instead of the default spherical coordinates. Option is also available to use open lateral boundary conditions using data from the European Center for Medium-Range Weather Forecast (ECMWF), Consortium for Small-Scale Modeling (COSMO) model, and the ICON model itself for limited-area simulations.

4. Benchmarking ICON-LES

Within the framework of HD(CP)^2, two simulations are performed to benchmark ICON as a model capable of doing large eddy simulations: the dry convective boundary layer (DCBL) and the cloud topped boundary

layer (CTBL). Both simulations are performed in a doubly periodic domain with prescribed surface fluxes and zero flux at the top. The model configuration of ICON capable of performing LES is termed as ICON-LES (hereafter simply ICON). The setups used here have been studied extensively in the literature, both numerically and experimentally (see e.g., *Deardorff* [1972]; *Willis and Deardorff* [1974]; *Moeng* [1984]; *Wyngaard* [1985]; *Schmidt and Schumann* [1989] and the references therein for DCBL, and *Nitta and Esbensen* [1974]; *Sommeria* [1976]; *Nicholls and LeMone* [1980]; *Siebesma and Cuijpers* [1995]; *Stevens* [2007], and the references therein for CTBL). For this reason and because they test the representation of dry convective turbulence and its coupling to the moist processes, they are good candidates for benchmarking LES models simulating atmospheric boundary layer turbulence.

To further assist the benchmarking process, simulations are also performed using two well-established and standard LES models: (a) UCLA-LES [*Stevens et al*., 2005] (hereafter simply UCLA) and (b) PALM [*Raasch and Schröter*, 2001; *Maronga et al*., 2015]. The numerics in ICON and the standard LES models differ significantly because of the differences in the underlying grid. Some of the major differences in the model dynamics, which we think will be helpful in understanding the differences in the subsequent sections, are listed below:

1. ICON uses the fully compressible set of equations whereas UCLA uses the anelastic approximation [*Ogura and Phillips*, 1962] and PALM uses the Bousinessq approximation [*Dutton and Fichtl*, 1969]. Therefore, ICON is forced to use a smaller time step allowing for the sound-wave propagation. For the simulations performed here, the dynamical time step in ICON is about 0.02 times that of PALM and UCLA.
2. ICON solves the edge-normal velocity component, therefore it has three degrees of freedom in each grid cell whereas it is four in the UCLA and PALM.
3. ICON uses θ_ρ as the prognostic variable for the thermodynamic equation, whereas UCLA and PALM use θ_l as the prognostic variable.
4. ICON uses q_v and q_l as the prognostic variables to represent moist processes, whereas UCLA and PALM use q_t that is a conserved quantity in the absence of precipitation.
5. The advection scheme for momentum equations in ICON is second-order accurate in both vertical and horizontal directions. In addition, ICON uses fourth-order artificial numerical dissipation for numerical stability in the momentum equations. In UCLA and PALM, the momentum advection schemes are fourth-order central and fifth-order upwind, respectively.
6. The advection scheme for the thermodynamic equation in ICON uses the second-order upwind [*Miura*, 2007] and central scheme for flux reconstruction in horizontal and vertical directions, respectively. In addition, a Smagorinsky type second-order numerical dissipation is applied on temperature fields for stability reasons. In UCLA and PALM, these are second-order (with flux limiter) and fifth-order upwind, respectively.
7. The tracer advection scheme in ICON uses the second-order upwind scheme by *Miura* [2007] in horizontal (there is an option for third-order upwind also) and third-order piecewise parabolic method by *Colella and Woodward* [1984] in vertical direction with flux limiter. In UCLA and PALM, these are second-order (with flux limiter) and fifth-order upwind, respectively.
8. ICON uses a second-order Predictor-Corrector time integration [*Zängl et al*., 2014] scheme whereas UCLA and PALM both use a third-order Runge-Kutta scheme.
9. ICON and UCLA use the classical Smagorinsky turbulence scheme whereas PALM uses the turbulent kinetic energy based scheme of *Deardorff* [1980].

In addition to the artificial numerical dissipation, a three-dimensional divergence damping of fourth-order is used in ICON to damp the acoustic waves. The damping coefficient is set to $0.0025\Delta t$. It is advisable for LES simulations to minimize the use of dissipation so that it does not interfere with the subgrid diffusion. However, the use of the artificial dissipation cannot be avoided for simulations with real orography, therefore, we decided to switch it on to see its effect on the resolved scales in the benchmark cases.

The points mentioned above clearly show the advantages that standard LES models (like UCLA and PALM) have over the general purpose models like ICON, which must be kept in mind while analyzing the results presented in the subsequent sections. A summary of the formal accuracy of the (advection) schemes used in these models is provided in Table 1.

Table 1. Formal Order of Accuracy of the Schemes Used in the Discretization of the Various Advective Terms in ICON, UCLA, and PALM

Model	Momentum (Horizontal, Vertical)	Thermodynamics (Horizontal, Vertical)	Tracer (Horizontal, Vertical)
ICON	(2,2)	(2,2)	(2,3)
UCLA	(4,4)	(2,2)	(2,2)
PALM	(5,5)	(5,5)	(5,5)

4.1. Dry Convective Boundary Layer

4.1.1. Simulation Design

The dry convective boundary layer simulation is initiated with a potential temperature profile constantly increasing with height from a surface temperature of $\theta_s = 290$ K at a constant lapse rate of $\Gamma = 0.006$ Km^{-1}. The initial wind is set to zero and the turbulence is triggered by adding random perturbations to the temperature field up to a height of 300 m in ICON and up to 1600 m in UCLA and PALM. The boundary layer then develops in time because of the fixed kinematic surface heat flux $(\overline{w'\theta'})_s$=0.1 K ms^{-1}. Note that the *overbar* $\overline{()}$ henceforth denotes spatial average over horizontal slabs of the computational domain and the prime $()'$ is used to indicate the deviation from this slab average. Kinematic units are used to force the models with the same surface fluxes irrespective of the way density is handled by them individually.

Simulations are performed for 3 h on a domain of size 9.6 $\times$ 9.6 km^2 in horizontal and 3.2 km in the vertical with varying grid spacings to study grid convergence. Resolutions considered for the present case are ($\Delta x = \Delta y = \Delta z = \Delta$): (a) 100 m, (b) 50 m, and (c) 25 m. Ascribing similar grid resolution to a triangular mesh is not possible. In practice, either the length between the two cell-centers or the length of the triangle edge or the square root of the area of the triangle is used to identify the grid resolution. Following the latter, and noting that the triangles in a doubly-periodic flat plane are equilateral, the triangle edge length (Δl) corresponding to the resolution (Δx,Δy) of a regular grid cell is obtained by equating the area of the cells in the two grids:

$$\Delta l \approx 1.5\sqrt{\Delta x \Delta y}\,. \tag{38}$$

This definition ensures the same number of grid cells in both meshes. However, the spectral analysis of the simulation data revealed that the actual grid resolution is lower than the present estimation. This is discussed further in Appendix C. It is also worth noting that the same number of grid cells in both triangular and rectangular meshes implies less degrees of freedom in ICON, which has three velocity components per grid cell, compared to the rectangular mesh, which has four velocity components per grid cell.

4.1.2. Time Evolution

We start by analyzing the time evolution of the horizontal mean of boundary layer height as simulated by the three models in Figure 3. It is calculated as the height (z_i) at which the vertical gradient of θ is at maximum. Different model resolutions are indicated in each figure. The jumps in z_i during the first 30–75 min (progressively less for higher resolutions) indicate the spin-up phase during which turbulence is first establishing itself. The difference in UCLA and PALM as compared to ICON is because of differences in initialization (i.e., the height of initially prescribed random noise). ICON shows large oscillations for $\Delta = 100$ m while keeping the (temporal) mean lower than the other LES models. One clear feature that is seen in these results, which has been noted previously, e.g., by *Sullivan and Patton* [2011], is that the entrainment rate (dz_i/dt) decreases in all the models as the grid spacing Δ is reduced. The effect of the larger entrainment rate at coarse resolution is seen as enhanced warming in Figure 4.

4.1.3. Vertical Structure

Vertical profiles of θ, averaged spatially over the horizontal domain and temporally over the last 15 min of the simulation (sampled every 30 s), are shown in Figure 4. For $\Delta = 100$ m, ICON captures the gross features, like the superadiabatic layer near the surface and the interfacial layer, just like standard LES models. The profile changes appreciably as the resolution is increased and ICON remains trustful to what are by now familiar patterns, e.g., as shown by the UCLA and PALM. UCLA entrains more (see Figure 6 near z_i), the effect of which is more heating in the mixed layer and a deeper interfacial layer. At $\Delta = 12.5$ m, the θ profile in PALM and UCLA (not shown) does not change much indicating a nearly converged solution at $\Delta = 25$ m. This can be also realized in Figure 5 where the convergence of horizontally averaged θ at the boundary layer height (calculated at the end of simulation) with increasing resolution is shown. From the

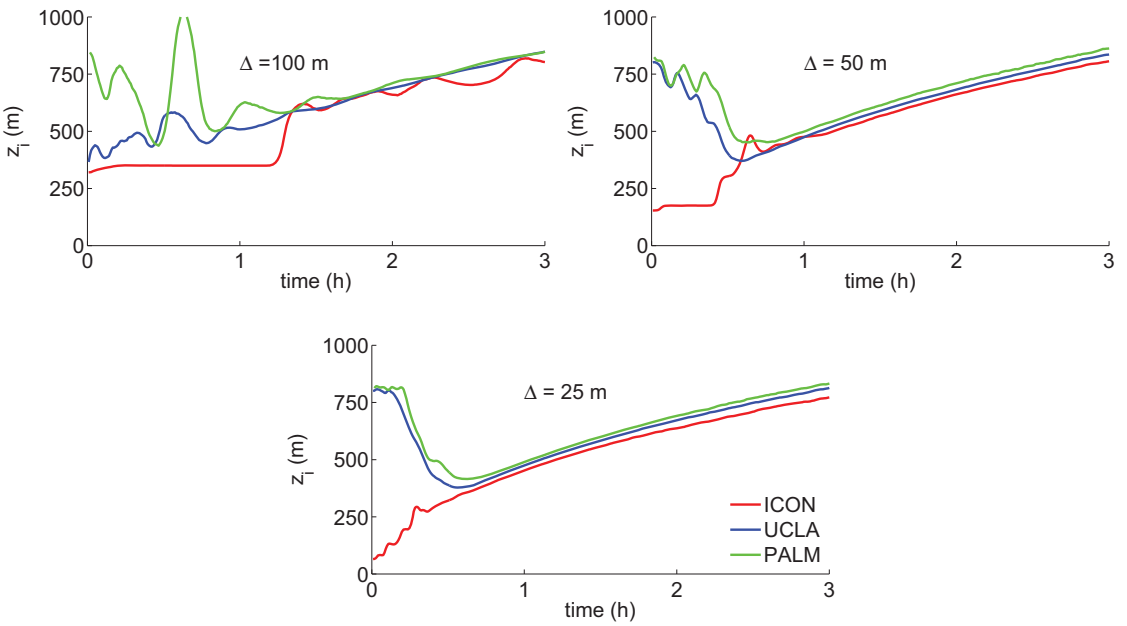

Figure 3. Time evolution of boundary layer height at the indicated resolutions.

figure it is clear that all the models approach convergence at the same rate with ICON following PALM more closely.

The subgrid contribution to the total flux should decrease with increasing resolution, so that the resolved and the total flux coincide except near the surface and inversion. To study this, the total and subgrid part of the mean vertical turbulent heat flux is plotted in Figure 6 for different resolution. The resolved flux in ICON is obtained as

$$\overline{w'\theta'} = \overline{w\theta} - \bar{w}\bar{\theta}\,, \tag{39}$$

which leads to some diagnostic error which is visible as a small bump near the surface in all the panels (e.g., at z = 100 m in the middle panel). The other models avoid such errors by directly using the advective fluxes as the resolved scale fluxes, because $\bar{w} \equiv 0$ due to incompressibility and periodicity.

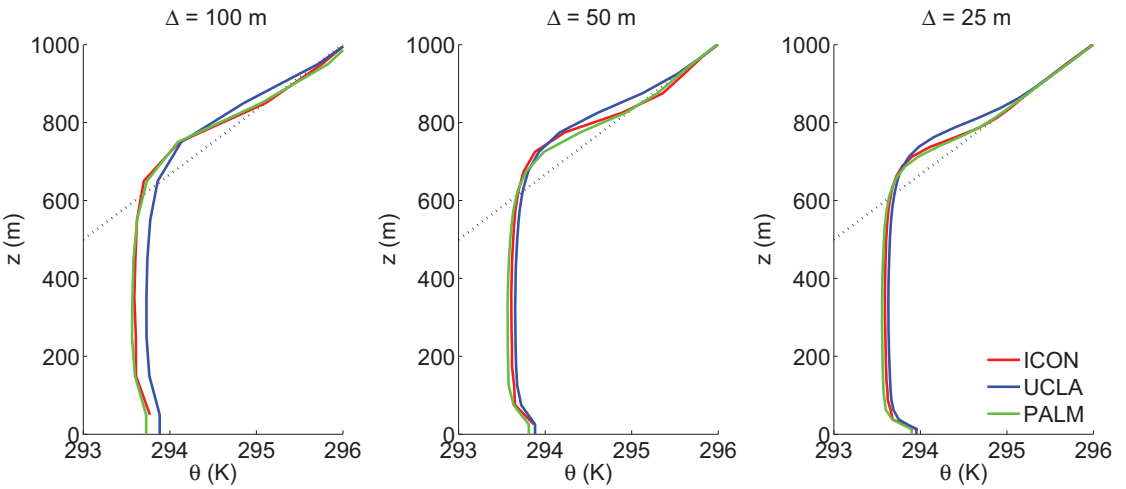

Figure 4. Vertical profile of mean potential temperature at the indicated resolutions. The dashed line is the initial profile.

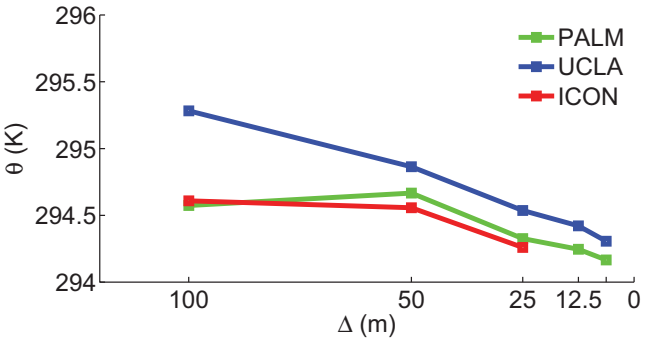

Figure 5. Mean potential temperature at the boundary layer height with increasing resolution.

At $\Delta = 100$ m, PALM has a small (positive) heat flux immediately above the inversion which is not seen for the other models. This is an artifact indicative of insufficient numerical damping in the PALM model. A similar pattern was found in *Moeng* [1984] who used a central difference scheme in the vertical. The subgrid-scale flux in ICON is almost the same as in UCLA because they use the same turbulence scheme, whereas it is slightly smaller in PALM, at all resolutions. As expected, subgrid-scale fluxes of ICON (and other models) decrease, hence the resolved scale fluxes increase, as the resolution is increased. In general, PALM shows the highest turbulent flux in the surface layer. At the inversion, $\overline{w'\theta'}$ in ICON and PALM are about 10% of the surface value (at all resolutions), whereas it is about 18% in UCLA. These values are within the expected range of 10–30% [*Stull*, 1988, p. 478]. The deeper and (negative) stronger inversion in UCLA explains its larger cooling rate in the inversion layer in Figure 4 [*Garcia and Mellado*, 2014].

Previous model intercomparison studies have shown that significant spread exists between models for vertical velocity variance ($\overline{w'^2}$) [*Siebesma et al*., 2003; *Stevens et al*., 2001]. In order to quantitatively assess $\overline{w'^2}$, we have used the DNS results of *Garcia and Mellado* [2014] for reference in Figure 7. Although the subgrid contribution to $\overline{w'^2}$ is missing in the LES models (because of its unavailability from ICON), we have noted from UCLA and PALM that its contribution is fairly small to affect the discussions below. In order to dimensionalize the DNS results, $z_i = 700$ m and a convective velocity scale $w_* = [(g/\theta_s)(\overline{w'\theta'})_s z_i]^{1/3} = 1.33$ ms^{-1} from ICON results at $\Delta = 25$ m are used.

$\overline{w'^2}$ is somewhat underestimated by all the models at $\Delta = 100$ m, except for ICON and UCLA which overestimate it above z = 400 m and z = 600 m, respectively. At $\Delta = 50$ m, all models underestimate the variance below z $\approx$ 200 m. Beyond z = 400 m, ICON and UCLA overestimate the variance whereas PALM underestimates it. At the highest resolution, PALM correctly captures the variance throughout the boundary layer, except with an overestimation near the top. At this resolution, both ICON and UCLA show an improvement for z < 200 m but they overestimate the DNS above 200 m. This consistent overestimation by ICON and UCLA can be understood by noting that in the absence of mean (horizontal) wind and subsidence,

$$\frac{\partial \overline{w'^2}}{\partial t} = \frac{2g\overline{w'\theta'_\rho}}{\overline{\theta_\rho}} + \text{other terms}, \tag{40}$$

for the present case. By closely inspecting Figure 6, we note that $\overline{w'\theta'}$ (= $\overline{w'\theta'_\rho}$ for DCBL) is also overestimated by ICON and UCLA in a similar manner.

Results in this section suggest that ICON performs satisfactorily in comparison to UCLA and PALM. For $\Delta = 100$ m, ICON captures the salient features of the boundary layer better than the models run at a few km resolution without parameterized boundary layers (e.g., cloud resolving models). ICON also shows grid convergence which is necessary to ensure the consistency of the discrete system. We focused on the vertical heat flux to tune the value of the Smagorinsky constant, and $C_s \sim 0.2$ was found to give the best results. The model became unstable for $C_s < 0.11$. We also performed simulations using $\frac{1}{\lambda} = \frac{1}{C_s\Delta} + \frac{1}{\kappa x_3}$, instead of equation (11), to get reduced values of K_m and K_h near the surface. The fluxes did improve near the surface but we also saw wiggles near the surface in the mean profile of temperature, so we decided to stay with equation (11).

4.1.4. Spatial Structure

It is also instructive to look at the spatial structure of the flow field for better assessment of the model. The most commonly known spatial feature in convective boundary layers is the presence of a spoke-like pattern near the surface [*Mason*, 1989; *Schmidt and Schumann*, 1989]. In order to find out whether ICON can resolve such a pattern on its triangular grid, contours of the fluctuations of the virtual potential temperature and

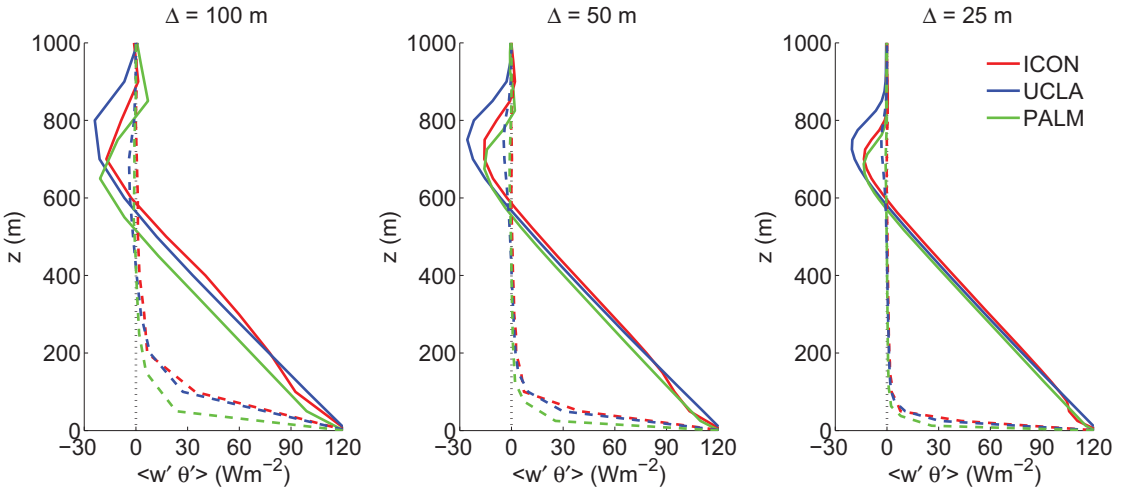

Figure 6. Mean vertical heat flux profile at the indicated resolutions. The solid lines are the total and the dashed lines are the subgrid-scale part of the total flux. The zero value is indicated by dashed line.

vertical velocity in a horizontal cross section are plotted in Figure 8 for $\Delta = 25$ m. The figures clearly show those spoke-like patterns in both w' and θ'_ρ contours. By visually inspecting the figure, we find that the typical length of the segments forming this pattern is about $1.3z_i$, similar to the value reported in *Schmidt and Schumann* [1989]. As expected, w' and θ'_ρ are strongly correlated as required by the sign of vertical heat flux.

4.2. Cloud Topped Boundary Layer

4.2.1. Simulation Design

For the benchmarking of ICON as an LES model it is necessary to ensure that it correctly represents the strong nonlinearity of moist processes. This is achieved by including (nonprecipitating) clouds in a setup otherwise similar to that for the dry convective boundary layer. We follow the idealized setup of cumulus convection described in *Stevens* [2007]. The simulation has been initialized with the same conditions as the DCBL case to carefully examine the effect of moist convection as opposed to the dry case. In addition, moisture is initialized with an analytic profile for specific humidity given by

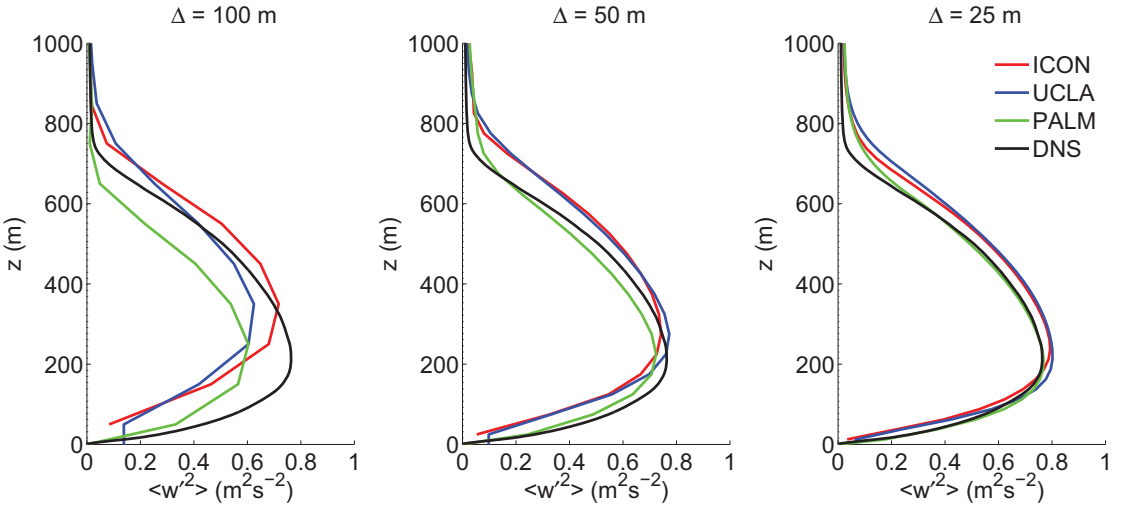

Figure 7. Mean vertical velocity variance profile (resolved) at the indicated resolutions together with a reference DNS profile.

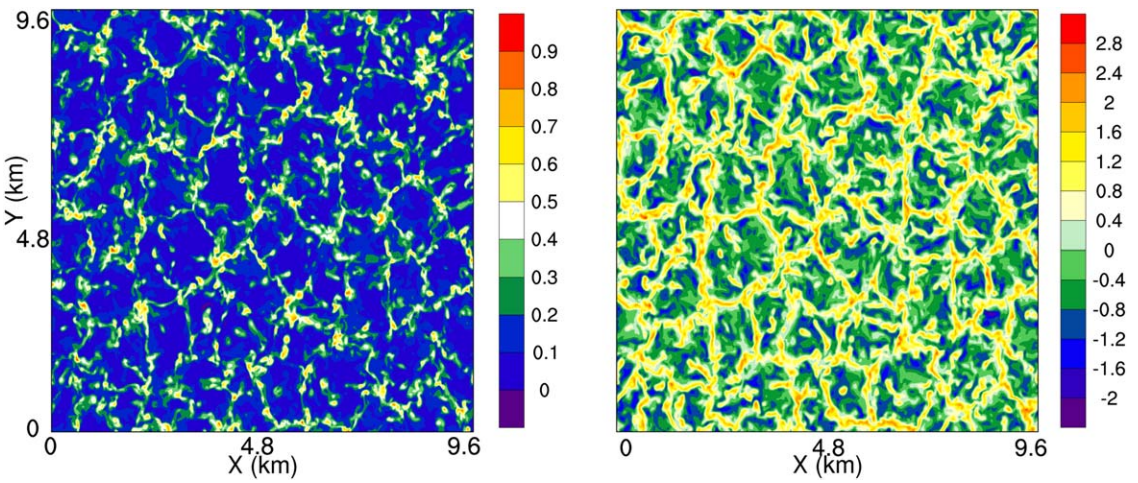

Figure 8. Contour plots of (left) θ'_ρ (K) and (right) w' (ms^{-1}) in a horizontal plane at z = 137 m drawn at the end of the simulation for $\Delta = 25$ m.

$$q_v(z) = 0.0088 \exp(-z/1500)\,. \tag{41}$$

The factor 0.0088 is roughly 0.74 times the saturation specific humidity at the surface. This profile corresponds to an exponentially decreasing relative humidity, which in turn ensures an initial equivalent potential temperature profile decreasing with height which is necessary for the growth of a conditionally unstable cloud layer [*Stevens*, 2007]. The initial temperature and humidity profiles are shown in Figures 10a and 10b as dotted lines. The initial wind is set to zero as in the DCBL case.

Similar to the DCBL, the boundary layer is set to grow in time due to a fixed forcing at the surface. Instead of fixing the sensible and the latent heat flux at the surface, an extra degree of freedom is provided to the system by allowing these fluxes to change in time while maintaining a constant surface buoyancy flux $B = \frac{g}{\Theta}(\overline{w'\theta'_\rho})_s = 0.0007$ m^2 s^{-3} for the reference temperature $\Theta = 290$ K. The surface thermodynamic variables, θ_s and q_{vs} are obtained by iterating the following equation:

$$B = \frac{g}{\Theta} C|\mathbf{v_h}(\Delta z))|[(\theta_s - \bar{\theta}(\Delta z)) + \epsilon\bar{\theta}(\Delta z)(q_{vs} - \overline{q_v}(\Delta z))], \tag{42}$$

where $q_{vs} = q_{sat}(p_s, \theta_s(\frac{p_s}{p_{00}})^{R_d/c_{pd}})$ is the saturation humidity at surface pressure $p_s = 1020$ hPa. Here $\bar{\theta}(\Delta z)$ and $\overline{q_v}(\Delta z)$ are the horizontally averaged potential temperature and specific humidity at the first model level, and $\epsilon = R_d/R_v - 1$. The turbulent exchange coefficient, $C|\mathbf{v_h}(\Delta z)|$, has been fixed to 0.02 ms^{-1} in all the models. For a typical value of the transfer coefficient C ($\sim$0.001–0.002) over sea surface at low wind speed [*Beljaars*, 1994], $C|\mathbf{v_h}(\Delta z)| = 0.02$ ms^{-1} implies very high wind speed of order 10 ms^{-1}. Such large wind speeds are unrealistic, but because they only serve to determine the surface fluxes, this only effects the strength of the near surface gradients of temperature and moisture.

Results in the previous section clearly show convergence of ICON as the grid resolution is increased. The intermediate resolution of $\Delta = 50$ m was found to be in good agreement with $\Delta = 25$ m. Similar conclusion was drawn for the CTBL case with a base simulation using $\Delta = 50$ m and another simulation with double the number of points in the vertical. It is for this reason that we only use the results from the base simulation in this section. The domain size is kept the same as in the dry case with doubly periodic boundary conditions and the solution is integrated for 25 h.

4.2.2. Time Evolution

Figure 9a shows the time evolution of the boundary layer height as simulated by the three models. As noted earlier in Figure 3, UCLA and PALM start with a big jump due to the random initialization. Before the cloudy layer develops, the evolution of z_i in all the models is consistent with the DCBL case at $\Delta = 50$ m in the sense that ICON has lowest z_i and PALM has the highest. UCLA and PALM match well until t = 20 h after which they depart slowly. ICON simulates a shallower boundary layer (by 150–200 m). The rate of boundary layer growth, $\frac{dz_i}{dt}$, in ICON (and in both other models) increases due to the developing cloud layer after

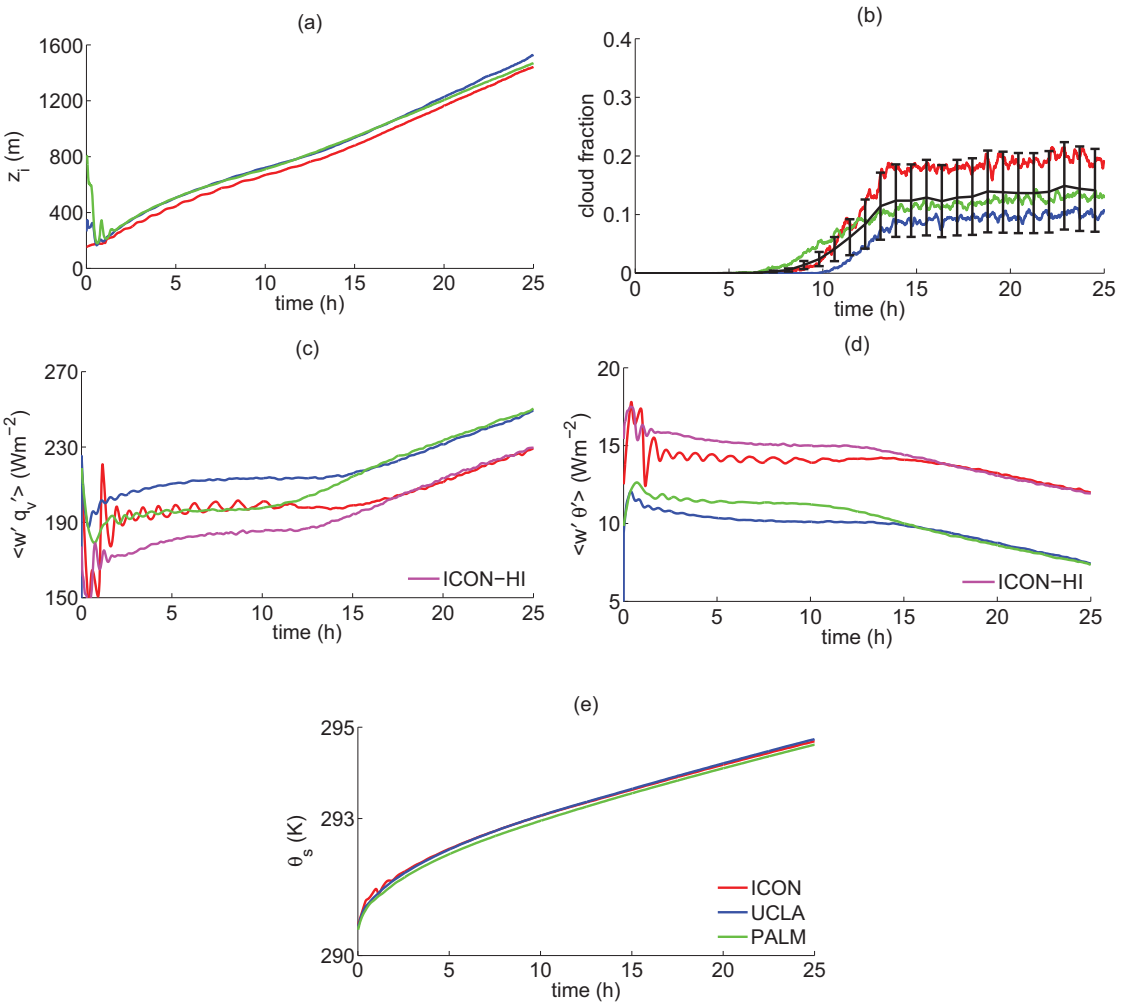

Figure 9. Time evolution of the indicated quantities for the cloud topped boundary layer simulation. The black solid line in Figure 9b is the mean over all the three models used in the present paper, and the spread of 50% [from *Siebesma et al.*, 2003] about this ensemble mean is indicated by the bars. The magenta lines in Figures 9c and 9d are from ICON after doubling the number of vertical levels.

≈12 h. This is consistent with earlier findings [*Stevens*, 2007] that $\frac{dz_i}{dt}$ varies as $t^{1/2}$ when the boundary layer is dry, and as t when the cloud layer develops.

Clouds are triggered at t ≈ 5 h in ICON and PALM, and at t ≈ 10 h in UCLA as seen in Figure 9b. All models maintain a near constant cloud fraction after t = 15 h. ICON saturates at a cloud fraction of 0.2, PALM at 0.13, and UCLA at 0.1. In order to ensure that the spread in cloud fraction lies within the known limits of uncertainty due to different model configurations, an uncertainty range is added in the figure corresponding to the spread found in the LES intercomparison study of cumulus convection as observed during the Barbados Oceanographic and Meteorological Experiment (BOMEX) by *Siebesma et al.* [2003]. The range shows a spread of 50% about the ensemble mean which is marked as a thin solid line. It is clear that all the models stay within this range despite all the differences.

The surface temperatures in all the models match quite well, except for some initial oscillations in ICON (see Figure 9e). These oscillations are more apparent in the surface fluxes in Figures 9d and 9e for t < 10 h. At first we thought that the oscillations are due to the fact that ICON has lesser degree of freedom than UCLA and PALM, therefore we did simulations with higher horizontal resolution so that the degree of freedom in ICON becomes equal to the other models (see discussions in Appendix C) and also with doubled vertical resolution ($\Delta_3 = 25$ m). Simulation with higher horizontal resolution had minimal effect (not shown). Simulation with doubled vertical resolution, as indicated by *ICON–HI* in Figures 9c and 9d, show that the

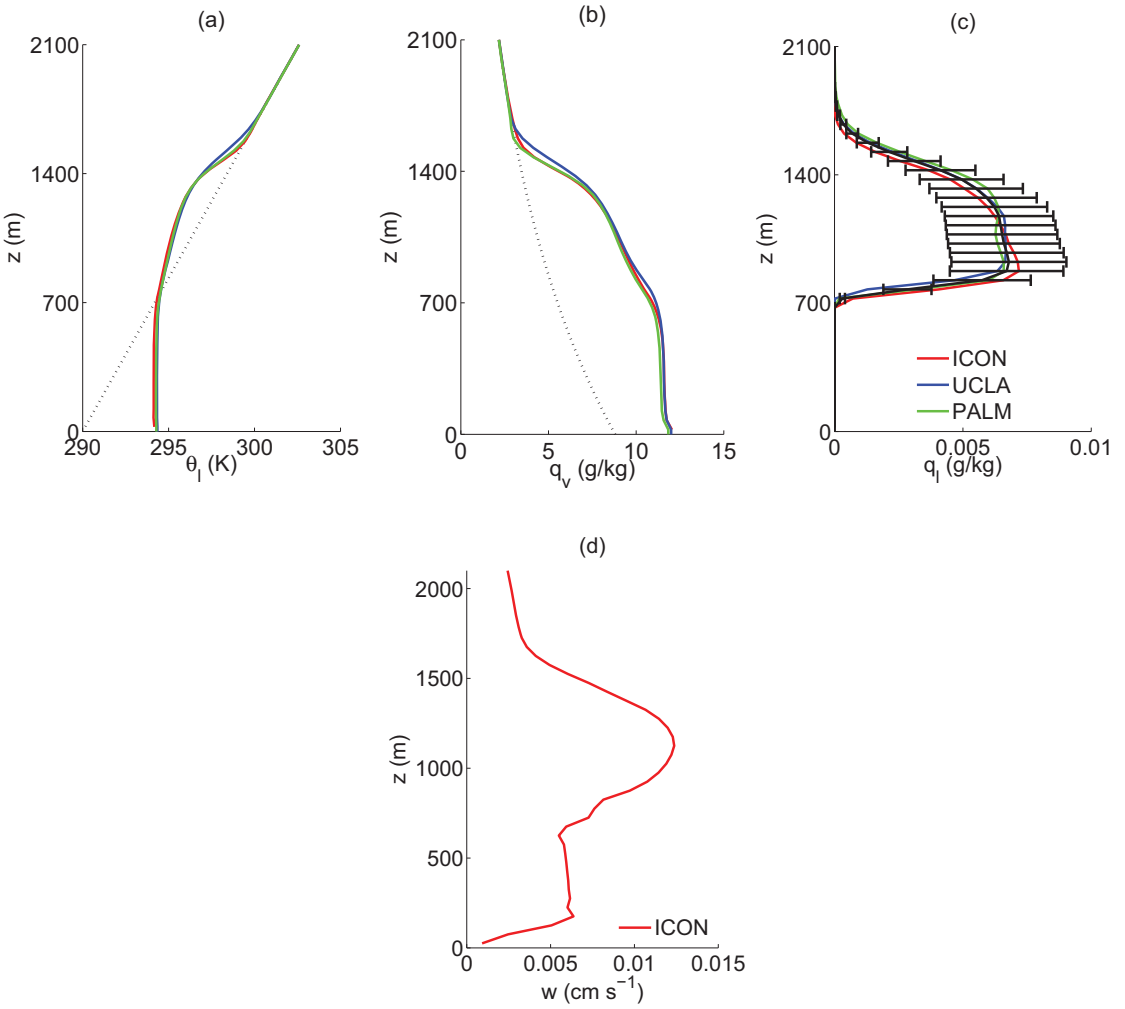

Figure 10. Mean vertical profiles of (a) θ_l, (b) q_v, (c) q_l, and (d) w. The initial conditions are indicated by the black dashed lines, and the black solid line in Figure 10c is the mean over the three models and the uncertainty range from *Siebesma et al.* [2003].

oscillations are greatly reduced in ICON suggesting that the oscillations are mainly due to grid-locking of the inversion height to model levels.

Besides these initial oscillations, the surface fluxes in the models evolve in the same fashion. ICON simulates higher $(\overline{w'\theta'})_s$ (by 5 W m^{-2}) throughout the simulation and smaller $(\overline{w'q_v'})_s$ (by 20 W m^{-2}) after the formation of the clouds, thereby maintaining a constant value of the buoyancy flux.

4.2.3. Vertical Structure

In this section we look at the vertical structure of the thermodynamic variables and the turbulent fluxes in ICON. The vertical profiles are obtained by averaging spatially in the horizontal direction and temporally over the last 30 min (sampled every 30 s). The liquid water potential temperature ($\overline{\theta_l}$) profile in Figure 10a shows that ICON is about 0.2 K cooler compared to UCLA in the subcloud layer. Similar behavior was seen in the DCBL case. We believe that this additional cooling in ICON is due to the fact that a fraction of the heat transported from the surface is used in the expansion work in ICON, thereby generating mean vertical wind (see Figure 10d), which does not take place in the other two models because of the Bousinessq and anelastic assumptions. Furthermore, the subcloud layer top in ICON is slightly less than 700 m where UCLA and PALM converge. This implies a shallower cloud base in ICON which can also be seen in the q_l profile in Figure 10c. The specific humidity profile from ICON lies exactly between that of PALM and UCLA as seen in Figure 10b.

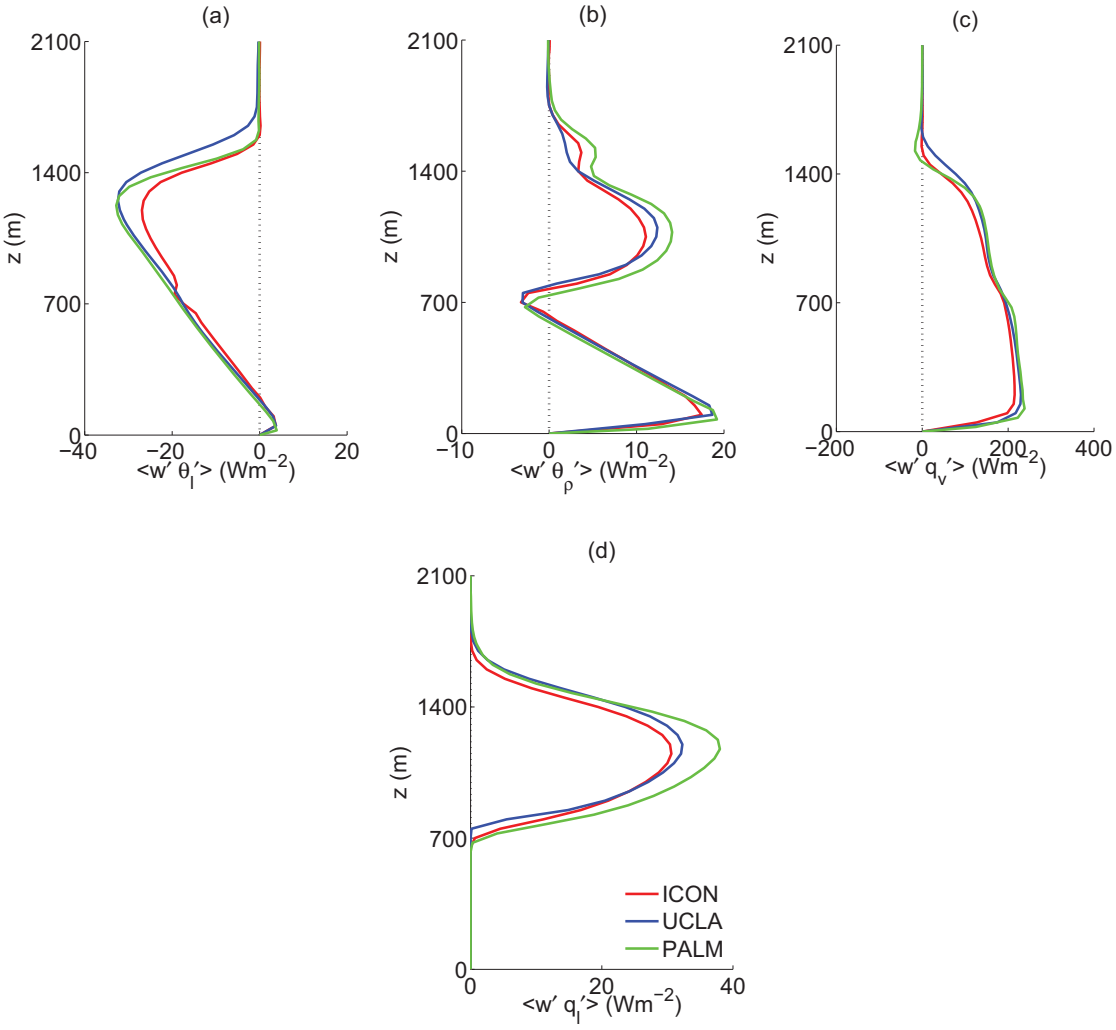

Figure 11. Turbulent flux (resolved) profiles of the indicated quantities in the cloud topped boundary layer simulation. The zero value is indicated by black dashed line.

As previously mentioned, ICON prognoses both q_l and q_v whereas PALM and UCLA only prognose q_t. q_c is then diagnosed using the condensation scheme of *Sommeria and Deardorff* [1977]. Despite this difference, the mean cloud liquid water in ICON stays within the range noted earlier by *Siebesma et al*. [2003], as indicated by the bars in Figure 10c. The reason for a lower cloud base in ICON can be understood by realizing that the air near the surface in ICON is moister than in the other models (by 0.2g kg^{-1}) whereas the temperature is a little lower (by 0.2 K). Therefore, an air parcel ascending from the surface saturates much faster in ICON in comparison to PALM and UCLA. Furthermore, the slightly lower cloud top in ICON suggests enhanced mixing with the dry atmosphere above, in comparison to other models. This extra mixing near the cloud top in ICON is either due to the implicit diffusion in the tracer advection scheme or the flux limiter which gets more active near the cloud boundary in ICON because of the use of nonconservative tracers.

The lower maximum (negative) $\overline{w'\theta_l'}$ flux in ICON as seen Figure 11a is because of lower liquid water vertical flux ($\overline{w'q_l'}$) (see Figure 11c), which can be understood by noting that

$$\overline{w'\theta_l'} = \overline{w'\theta'} - \frac{1}{\pi}\frac{L_v}{c_{pd}}\overline{w'q_l'}\,.$$

Figure 11a also shows a small kink at the cloud base in ICON. This is probably due to the use of the nonconservative thermodynamic and moisture variables in ICON which creates a discontinuity at the cloud

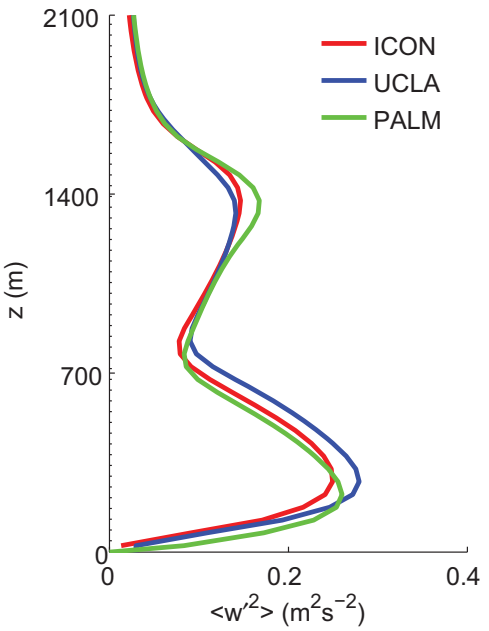

Figure 12. Vertical velocity (resolved) variance in the cloud-topped boundary layer simulation.

boundary. This effect, although very small in the present case, can generate significant errors in cases with strong convection.

The turbulent buoyancy flux in the subcloud layer of a CTBL is known to follow the DCBL case in a nondimensional sense [*Stevens*, 2007]. The maximum resolved buoyancy flux in DCBL case for $\Delta = 50$ m was found to be around 84% of the surface flux prescribed in all models. Looking at the similar maxima in Figure 11b (near the surface) it appears that ICON resolves slightly less, around 76% of the prescribed value ($(\overline{w'\theta'_\rho})_s = 25$ W m^{-2}) whereas UCLA and PALM resolve nearly 84%. However, as was mentioned during the discussion of Figure 6, this is simply a diagnostic error which arises due to the vertical averaging of the fluxes in ICON from main levels to the interface levels for plotting purposes. Also, Figure 11b shows two (positive) peaks as one would expect in a CTBL. The flux decreases linearly in the subcloud layer up to the cloud base where it resolves about 10% (negative) of $(\overline{w'\theta'_\rho})_s$ in all models.

The resolved vertical flux of specific humidity in ICON is found to be smaller than in the other two models (see Figure 11c). In the subcloud layer it is a consequence of its lower surface moisture flux, whereas in the cloud layer it is probably due to the enhanced mixing near the cloud top in ICON. The liquid water vertical flux ($\overline{w'q'_l}$) in ICON compares very well with other models (see Figure 11d) despite the aforementioned differences in the way cloud liquid water is handled.

Vertical profiles of resolved vertical velocity variance by the three models are shown in Figure 12. Similar to the dry case in Figure 7 for $\Delta = 50$ m, $\overline{w'^2}$ in ICON and UCLA are nearly the same till the lowest peak at $z \approx 300$ m. At the peak and beyond that, the variance in ICON is slightly smaller than in UCLA in the subcloud layer, which is different from the dry case. In the cloud layer and above, the differences between the two is reduced again.

Overall, the results of the CTBL simulation show that ICON follows the expected trend and agrees well with the standard LES models with some differences in and around the cloud layer. We believe that such differences are bound to show up because of the inherent differences in the model and experimental designs. Some of the differences in both DCBL and CTBL cases are also because of the artificial initial profiles of temperature and moisture that produces very thin boundary layer in the early phase of the simulation, which cannot be resolved with the prescribed grid resolution. While it is hard to argue how long and by how much this affects the simulation, we think that in the presented simulations such effects are relatively smaller after the first hour of the simulation. To confirm this, we also performed the BOMEX simulation [*Siebesma et al*., 2003] that does not suffer from similar initialization issues. The results from this case do not differ in any important way from those from the simulation of the CTBL case, and are therefore not presented here.

As already mentioned, several interpolations are required in ICON for spatial discretization which can lead to (numerical) errors and smoothening of the results. On top of that, unlike standard LES models that use high-order schemes for spatial discretization, the triangular grid in ICON poses a challenge on the use of higher-order schemes in the horizontal. It is, however, to be noted that the overall (spectral) accuracy of the models using such higher-order schemes decreases as the complexity of the experiment increases. For complex cases, the use of artificial second-order numerical dissipation becomes necessary to keep the model stable, which reduces the order of the leading truncation error term of the spatial discretization scheme to second order, thereby reducing the overall accuracy of the spatial discretization to first order [*Ghosal*, 1996].

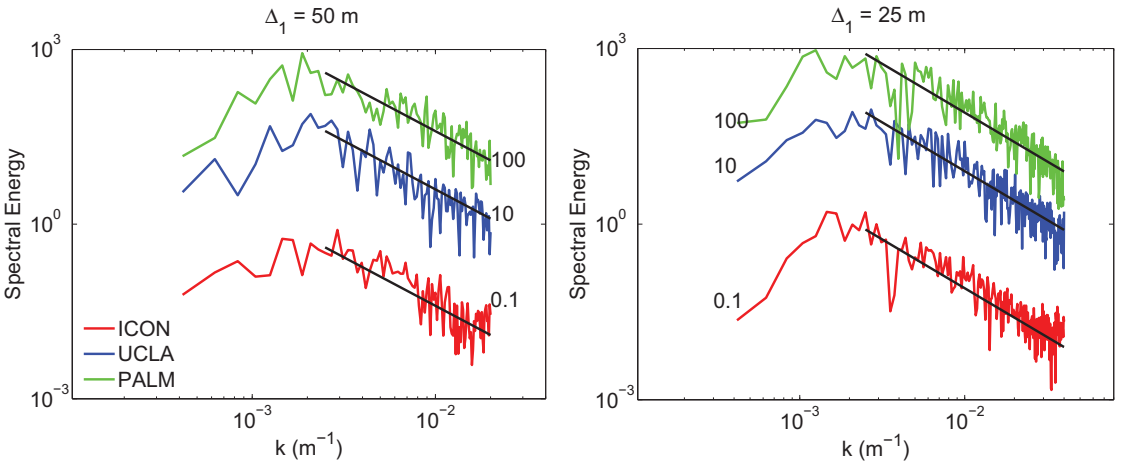

Figure 13. The horizontal spectra of the vertical velocity at indicated resolutions in log-log scale. The data have been multiplied by some factors in order to avoid overlap. Also shown is the expected Kolmogorov's spectrum ($\propto k^{-5/3}$) (black line), for $\Delta_1 = 50$, 25 m.

5. Conclusion

This paper describes the extension of a unified modeling system for climate and weather forecast ICON (ICOsahedral Nonhydrostic) to a large-eddy simulation framework and its comparison against two well-established LES models.

The first part details the implementation of the turbulence scheme on the triangular grid used in ICON and the numerical technique used to integrate the diffusion equations. Conservative implementation of a three-dimensional turbulence scheme in a triangular grid is nontrivial and involves several interpolation operations. Despite these computational overheads, the turbulence scheme in ICON-LES takes less than 20% of the overall computational time in case of a dry convective boundary layer, which is comparable to the performance of the similar turbulence scheme implemented in the quadrilateral grid of UCLA-LES.

The second part of the manuscript deals with the validation of ICON-LES against two standard LES models (UCLA-LES and PALM) for two test cases: dry convective boundary layer, and cloud-topped boundary layer. Considering the compromises that ICON undergoes from being a unified modeling system, and that it is mostly second-order accurate in space whereas UCLA-LES is fourth and PALM is fifth-order accurate, the eddy-resolving capability of ICON-LES is fairly good. The turbulence scheme in ICON-LES captures the mean

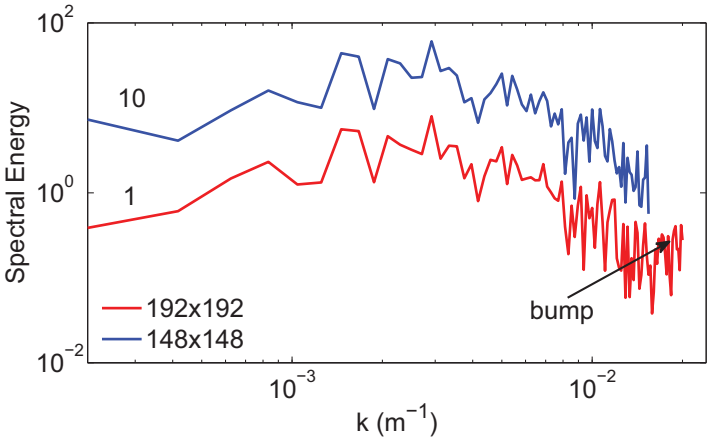

Figure 14. The horizontal spectra of vertical velocity at z = 500 m for two different grids.

flow characteristics quite satisfactorily, and produces similar turbulent structure and statistics in comparison to the standard LES models. In particular,

1. it was shown in section 4.1 that ICON-LES approaches toward a converged solution as the grid resolution is increased.
2. the profiles of resolved vertical fluxes for both DCBL and CTBL indicate that the eddy-resolving capabilities of ICON-LES is comparable to that of the standard LES models.
3. the lower cloud top in ICON-LES for the CTBL case suggests enhanced (numerical) mixing near the cloud top which could have been activated due to the use of nonconservative variables in ICON which creates a discontinuity at the cloud boundary.

Appendix A: Coupling of Dynamics and Turbulence

In this section, the sequential coupling of the dynamics with the turbulence parameterization in ICON is explained. When marching in time from $n\Delta t$ to $(n+1)\Delta t$, Δt being the physics time step, let us indicate the variables after being updated from dynamics by $()^{n+}$. Subgrid-scale diffusion is applied on equation (5) in three stages as following:

$$D_t v_1(v_1^{n+}, v_2^{n+}, ..)|_h = \frac{1}{\rho^{n+}}\left(\frac{\partial \tau_{11}^{n+}}{\partial x_1} + \frac{\partial \tau_{12}^{n+}}{\partial x_2}\right), \tag{A1}$$

$$D_t v_1(v_1^{n++}, v_1^{n+}, ..)|_v = \frac{\Delta_{x_3}\bar{K}^i_{\mathrm{m}}\left(\frac{\Delta_{x_3} v_1^{n++}}{\Delta x_3} + \frac{\Delta_{qp} v_3^{n+}}{\Delta_{qp} x_1}\right)}{2\Delta x_3}, \tag{A2}$$

$$\frac{v_1^{n+1} - v_1^{n+}}{\Delta t} = D_t v_1|_h + D_t v_1|_v . \tag{A3}$$

The RHS of equation (A1) is composed of the first two terms in equation (30), representing the horizontal diffusion, all evaluated using variables from dynamics. This equation is integrated in time using Euler explicit and the tendency is stored in $D_t v_1|_h$. Vertical diffusion is then performed using equation (A2) where all the terms in the RHS are also evaluated using the $()^{n+}$ variables, except for the term involving the vertical derivative of v_1, which is evaluated implicitly using Euler implicit method. This is indicated in equation (A2) by the use of an intermediate time step $n++$. The tendency from this equation is then combined with the horizontal tendency in the final equation to get the velocities at $(n+1)\Delta t$.

Subgrid-scale diffusion for the vertical momentum equation is similarly performed by splitting the RHS of equation (31) into the horizontal and vertical components. As for the thermodynamic and tracer variables, the implementation is described for θ following equation (32). That is,

$$D_t\theta(\theta^{n+})|_h = \frac{1}{a_c}\sum K_m \frac{\Delta_{qp}\theta^{n+}}{\Delta_{qp} x_1}\Delta_{cd} x_1 f_o, \tag{A4}$$

$$D_t\theta(\theta^{n++}, \theta^{n+})|_v = \frac{\Delta_{x_3}\left(\overline{K_m}^i \frac{\Delta_{x_3}\theta^{n++}}{\Delta x_3}\right)}{\Delta x_3}, \tag{A5}$$

$$\frac{\theta^{n+1} - \theta^*}{\Delta t} = D_t\theta(\theta^{n+})|_h + D_t\theta(\theta^{n++}, \theta^{n+})|_v . \tag{A6}$$

Here again, equation (A4) is integrated explicitly using the variables from dynamics and the tendency is stored in $D_t\theta|_h$, and equation (A5) is integrated implicitly storing the tendency in $D_t\theta|_v$. It is to be noted that K_m and K_h are always evaluated using the variables from dynamics.

Appendix B: Discretization of Turbulent Fluxes

Here we derive some of the turbulent fluxes on ICON grid for the interested readers.

Following steps are taken to derive equation (30). The first term on the RHS of above equation, which is due to the first term in the RHS of equation (29), is obtained as

$$\left.\frac{\partial \tau_{11}}{\partial x_1}\right|_e = \frac{\partial K_m (S_{11}-D)}{\partial x_1}|_e = \frac{\overline{K_m}^c|_p (S_{11}-D)|_p - \overline{K_m}^c|_q (S_{11}-D)|_q}{\Delta_{qp} x_1}$$
$$= \frac{\overline{K_m}^c|_p \left(\frac{\Delta_{eb} v_1}{\Delta_{eb} x_1} - \bar{D}^c|_p\right) - \overline{K_m}^c|_q \left(\frac{\Delta_{ae} v_1}{\Delta_{ae} x_1} - \bar{D}^c|_q\right)}{\Delta_{qp} x_1}$$
$$= \frac{\overline{K_m}^c|_p \left(\frac{\overline{v_1}^{ev}|_b - v_1|_e}{\Delta_{eb} x_1} - \bar{D}^c|_p\right) - \overline{K_m}^c|_q \left(\frac{v_1|_e - \overline{v_1}^{ev}|_a}{\Delta_{ae} x_1} - \bar{D}^c|_q\right)}{\Delta_{qp} x_1}.$$

The second term in RHS of equation (30) involves some manipulation which can be realized by noting that

$$\frac{\partial \tau_{12}}{\partial x_2}|_e = \frac{\partial K_m S_{12}}{\partial x_2}|_e = \frac{K_m|_f S_{12}|_f - K_m|_g S_{12}|_g}{\Delta_{gf} x_2}$$
$$= \frac{K_m|_f \left(\frac{\Delta_{ec} v_1}{\Delta_{ec} x_2} + \frac{\Delta_{li} v_2}{\Delta_{li} x_1}\right) - K_m|_g \left(\frac{\Delta_{de} v_1}{\Delta_{de} x_2} + \frac{\Delta_{kj} v_2}{\Delta_{kj} x_1}\right)}{2\Delta_{gf} x_2}$$
$$= \frac{K_m|_f \left(\frac{\overline{v_1}^{ev}|_c - v_1|_e}{\Delta_{ec} x_2} + \frac{v_2|_i - v_2|_l}{\Delta_{li} x_1}\right) - K_m|_g \left(\frac{v_1|_e - \overline{v_1}^{ev}|_d}{\Delta_{de} x_2} + \frac{v_2|_j - v_2|_k}{\Delta_{kj} x_1}\right)}{2\Delta_{gf} x_2}.$$

At this point, if we make the assumption that $K_m|_f = (K_m|_c + K_m|_e)/2$ and $K_m|_g = (K_m|_d + K_m|_e)/2$, and that v_2 at nodes i, j, k, l are also arithmetic averages of their neighboring vertices (e.g., $v_2|_i = (v_2|_c + v_2|_b)/2$), after some manipulation we end up with the second term of the RHS of equation (30). The third term on the RHS of equation (30) is a straightforward expansion of $\frac{\partial \tau_{13}}{\partial x_3}$ utilizing the strain rates located at $e_{k+1/2}$ and $e_{k-1/2}$ in Figure 2.

The first term on RHS equation (31), which is due to $\frac{\partial \tau_{31}}{\partial x_1}$, is evaluated at $e_{k-1/2}$ as (dropping out $_{k-1/2}$ for clarity)

$$\left.\frac{\partial \tau_{31}}{\partial x_1}\right|_e = \left.\frac{\partial K_m S_{31}}{\partial x_1}\right|_e = \frac{\overline{\overline{K_m}^c}^i|_p S_{31}|_p - \overline{\overline{K_m}^c}^i|_q S_{31}|_q}{\Delta_{qp} x_1}$$
$$= \frac{\overline{\overline{K_m}^c}^i|_p \left(\frac{\Delta_{eb} v_3}{\Delta_{eb} x_1} - \frac{\Delta_{x_3} v_1}{\Delta x_3}|_p\right) - \overline{\overline{K_m}^c}^i|_q \left(\frac{\Delta_{ae} v_3}{\Delta_{ae} x_1} - \frac{\Delta_{x_3} v_1}{\Delta x_3}|_q\right)}{\Delta_{qp} x_1}$$
$$= \frac{\overline{\overline{K_m}^c}^i|_p \left(\frac{\overline{v_3}^v|_b - \overline{v_3}^e|_e}{\Delta_{eb} x_1} + \frac{\Delta_{x_3} v_1}{\Delta x_3}|_p\right) - \overline{\overline{K_m}^c}^i|_q \left(\frac{\overline{v_3}^e|_e - \overline{v_3}^v|_a}{\Delta_{ea} x_1} + \frac{\Delta_{x_3} v_1}{\Delta x_3}|_q\right)}{2\Delta_{qp} x_1}.$$

Rest of the terms can be derived in a similar manner and are therefore not derived here.

Appendix C: Grid Resolution in ICON

It is mentioned at the outset that the results in this section are relevant for flat meshes only.

One of the difficulties with the triangular mesh is an a-priori estimation of its grid resolution (should not be confused with the effective grid resolution). For the present experiments, we have defined the resolution as square root of the area of the triangle, which gives

$$\Delta_1 = 0.67 \Delta l. \tag{C1}$$

The other two definitions which are frequently used are the distance between the two cell-centers, which gives

$$\Delta_2 = 0.58 \Delta l \tag{C2}$$

and, the triangle edge length that gives $\Delta_3 = \Delta\, l$. Of course, $\Delta_3 > \Delta_1 > \Delta_2$. An advantage of using the first definition is that it gives the same number of grid points as a regular mesh with an added disadvantage of having to deal with lesser degree of freedom per grid cell for velocity components. If one chooses to define a resolution such that the degrees of freedom remains the same as in a regular mesh, then for N_g number

of total grid points in a regular quadrilateral mesh, $\frac{4}{3}N_g$ grid points will be required in the ICON grid. Noting that the total number of grid points in an ICON grid is $2(L/\Delta l)^2$, for a square domain of length L, we can estimate the required resolution to be

$$\Delta_4 = \sqrt{\frac{2}{3}}\Delta l \approx 0.82\Delta l\,. \tag{C3}$$

In order to see how the estimation from equation (C1) compares with a regularly spaced grid model, we have compared the horizontal spectra of vertical velocity from ICON to that of PALM and UCLA for the DCBL case. These one-dimensional spectra are obtained by Fourier transforming the field along a horizontal line and averaging over all parallel lines at a fixed height and time. ICON spectrum is obtained by interpolating its velocity field to a regular grid with the same number of grid points as the standard LES models using distance weighted averaging technique. That is, the $\Delta_1 = 50$ m simulation results are interpolated to 192 $\times$ 192 grid points and the $\Delta_1 = 25$ m to 384 $\times$ 384 grid points. The corresponding spectra at z = 500 m are shown in Figure 13.

Figure 13 shows that the Kolmogorov's spectrum ($\propto k^{-5/3}$) is followed by all the models, and the representation of the larger scales improves as the resolution is increased to $\Delta_1 = 25$ m. The peculiarity of the ICON data is that it shows a small spectral bump toward the high wave numbers (see also Figure 14 where the ICON spectrum for $\Delta_1 = 50$ m is redrawn). This bump is indicative of aliasing in ICON data which lead to the accumulation of energy at the scales near the Nyquist limit. It means that 192 $\times$ 192 grid points is more than the actual number of points required to properly represent ICON data on a regular grid. After some trials with less number of grid points, we found that when interpolated to a 148 $\times$ 148 grid the bump in the spectrum almost disappears (see the blue colored line in Figure 14). This implies that 148 $\times$ 148 number of grid points in a regular grid is a fairly good representative of the ICON data at $\Delta_1 = 50$ m. We use this to infer that the spectral resolution of ICON grid is

$$\Delta_5 = \frac{192}{148}\Delta_1 \approx 0.87\Delta l\,. \tag{C4}$$

The estimate from equation (C4) cane be generalized further, accounting for the interpolation and measurement errors, to deduce that Δ_5 lies is the range of $0.8\Delta l - 0.9\Delta l$, which, at the best, is a good approximation. Interestingly, the resolution Δ_4 based on the degrees of freedom lies within the range of Δ_5. However, more investigation is required in this direction.

Acknowledgments

The authors thank the German Federal Ministry of Education and Research (BMBF) for their funding to support the HD(CP)^2 project (01LK1202E). We also thank Jade Garcia for providing us with the DNS data, the whole ICON development team at DWD and MPI-M for their excellent work, and the anonymous reviewers for their constructive suggestions. We specially thank Leonidas Linardakis for his continuous help during the course of the model development. The data used in this paper are available at the German Climate Computing Center and can be obtained from the corresponding author upon request.

References

Arakawa, A. (1966), Computational design for long-term numerical integration of the equation of fluid motion: Two-dimensional incompressible flow, Part I, *J. Comput. Phys.*, *1*, 119–143.

Beljaars, A. C. M. (1994), The parameterization of surface fluxes in large-scale models under free convection, *Q. J. R. Meteorol. Soc.*, *121*, 255–270.

Betts, A. K., and M. J. Miller (1986), A new convective adjustment scheme. Part II: Single column tests using GATE-wave, BOMEX, ATEX, and Arctic Airmass data sets, *Q. J. R. Meteorol. Soc.*, *112*, 693–710.

Bony, S., J. L. Dufresne, H. L. Treut, J. J. Morcrette, and C. Senior (2004), On dynamic and thermodynamic components of cloud changes, *Clim. Dyn.*, *22*, 71–86.

Bryan, G. H., J. C. Wyngaard, and J. M. Fritsch (2003), Resolution requirements for the simulation of deep moist convection, *Mon. Weather Rev.*, *131*, 2394–2416.

Chow, F. K., A. P. Weigel, R. L. Street, M. W. Rotach, and M. Xue (2006), High-resolution large-eddy simulations of flow in a steep alpine valley. Part I: Methodology, verification, and sensitivity experiments, *J. Appl. Meteorol. Climatol.*, *45*, 63–86.

Colella, P., and P. R. Woodward (1984), The piecewise parabolic method (PPM) for gas-dynamical simulations, *J. Comput. Phys.*, *54*, 174–201.

Deardorff, J. W. (1970), A numerical study of three-dimensional turbulent channel flow at large Reynolds numbers, *J. Fluid Mech.*, *41*, 453–480.

Deardorff, J. W. (1972), Numerical investigation of neutral and unstable planetary boundary layers, *J. Atmos. Sci.*, *29*, 91–115.

Deardorff, J. W. (1980), Stratocumulus-capped mixed layers derived from a three-dimensional model, *Boundary Layer Meteorol.*, *7*, 495–527.

Durran, D. R., and J. B. Klemp (1982), On the effects of moisture on the Brunt-Väisälä frequency, *J. Atmos. Sci.*, *39*, 2152–2158.

Dutton, J. A., and G. H. Fichtl (1969), Approximate equations of motion for gases and liquids, *J. Atmos. Sci.*, *26*, 241–254.

Garcia, J. R., and J. P. Mellado (2014), The two-layer structure of the entrainment zone in the convective boundary layer, *J. Atmos. Sci.*, *71*, 1935–1955, doi:10.1175/JAS-D-13–0148.1.

Gassmann, A., and H. Herzog (2008), Towards a consistent numerical compressible non-hydrostatic model using generalized Hamiltonian tools, *Q. J. R. Meteorol. Soc.*, *65*, 1597–1613.

Ghan, S., et al. (2000), A comparison of single column model simulations of summertime midlatitude continental convection, *J. Geophys. Res.*, *105*(D2), 2091–2124.

Ghosal, S. (1996), An analysis of numerical errors in large-eddy simulations of turbulence, *J. Comput. Phys.*, *125*, 187–206.

Grabowski, W. (2001), Coupling cloud processes with the large-scale dynamics using the cloud-resolving convection parameterization (CRCP), *J. Atmos. Sci.*, *58*, 978–997.
Grabowski, W., X. Xu, and M. W. Moncrieff (1996), Cloud-resolving modeling of topical cloud systems during phase III of GATE. Part I: Two-dimensional experiments, *J. Atmos. Sci.*, *53*, 3684–3709.
Hanley, K. E., et al. (2013), Mixing length controls on high resolution simulations of convective storms, *Q. J. R. Meteorol. Soc.*, *141*, 272–284, doi:10.1002/qj.2356.
Hinze, J. O. (1975), *Turbulence*, McGraw-Hill, N. Y.
Khairoutdinov, M., D. Randall, and C. Demott (2005), Simulations of the atmospheric general circulation using a cloud-resolving model as a superparameterization of physical processes, *J. Atmos. Sci.*, *62*, 2136–2154.
Lilly, D. K. (1962), On the numerical simulation of buoyant convection, *Tellus, XIV*, *2*, 148–172.
Louis, J.-F. (1979), A parametric model of vertical eddy fluxes in the atmosphere, *Boundary Layer Meteorol.*, *17*, 187–202.
Maronga, B., M. Gryschka, R. Heinze, F. Hoffmann, F. Kanani-Sühring, M. Keck, M. O. Letzel, S. Raasch, and M. Sühring (2015), The parallellized large-eddy simulation model (PALM) version 4.0 for atmospheric and oceanic flows: model formulation, recent developments, and future perspectives, *Geosci. Model Dev.*, *8*, 1539–1637, doi:10.5194/gmdd-8–1539-2015.
Mason, P. J. (1989), Large-eddy simulation of the convective atmospheric boundary layer, *J. Atmos. Sci.*, *46*, 1492–1516.
Mason, P. J., and A. R. Brown (1999), On subgrid models and filter operations in large eddy simulations, *J. Atmos. Sci.*, *56*, 2101–2114.
Miller, M. J. (1978), The Hampstead storm: A numerical simulation of a quasi-stationary cumulonimbus system, *Q. J. R. Meteorol. Soc.*, *104*, 413–427.
Miura, H. (2007), An upwind-biased conservative advection scheme for spherical hexagonal-pentagonal grids, *Mon. Weather Rev.*, *135*, 4038–4044.
Miura, H., M. Satoh, T. Nasuno, A. T. Noda, and K. Oouchi (2007), A Madden-Jullian Oscillation Event realistically simulated by a global cloud-resolving model, *Science*, *318*(5857), 1763–1765.
Moeng, C.-H. (1984), A large-eddy-simulation model for the study of planetary boundary layer turbulence, *J. Atmos. Sci.*, *41*, 2052–2062.
Moeng, C.-H., J. Dudhia, J. Klemp, and P. Sullivan (2007), Examining two-way grid nesting for large eddy simulation of the PBL using the WRF model, *Mon. Weather Rev.*, *135*, 2295–2311.
Narcovich, F., and J. Ward (1994), Generalized Hermite interpolation via matrix-valued conditionally positive definite functions, *Math. Comput.*, *63*, 661–687.
Nicholls, S., and M. A. LeMone (1980), The fair weather boundary layer in GATE: The relationship of subcloud fluxes and structure to the distribution and enhancement of cumulus clouds, *J. Atmos. Sci.*, *37*, 2051–2067.
Nitta, T., and E. Esbensen (1974), Heat and moisture budget analyses using BOMEX data, *Mon. Weather Rev.*, *102*, 17–28.
Ogura, Y., and N. A. Phillips (1962), Scale analysis of deep and shallow convection in the atmosphere, *J. Atmos. Sci.*, *19*, 173–179.
Patankar, S. V. (1980), *Numerical Heat Transfer and Fluid Flow, Comput. Methods Mech. Therm. Sci.*, McGraw-Hill, N. Y.
Raasch, S., and M. Schröter (2001), PALM—A large-eddy simulation model performing on massively parallel computers, *Meteorol. Z.*, *10*(5), 363–372.
Randall, D., K.-M. Xu, R. J. C. Sommerville, and S. Iacobellis (1996), Single-column models and cloud ensemble models as links between observations and climate models, *J. Clim.*, *9*, 1683–1697.
Sagaut, P. (1998), *Large Eddy Simulation for Incompressible Flows*, 3rd ed., Springer, Germany.
Satoh, M., et al. (2014), The non-hydrostatic icosahedral atmospheric model: Description and development, *Prog. Earth Planet. Sci.*, *1*(18), 1–32.
Schmidt, H., and U. Schumann (1989), Coherent structure of the convective boundary layer derived from large-eddy simulations, *J. Fluid Mech.*, *200*, 511–562.
Seifert, A., and K. D. Beheng (2001), A double-moment parameterization for simulating autoconversion, accretion and self collection, *Atmos. Res.*, *59–60*, 265–281.
Siebesma, A. P., and J. W. M. Cuijpers (1995), Evaluation of parameteric assumptions for shallow cumulus convection, *J. Atmos. Sci.*, *52*(6), 650–666.
Siebesma, A. P., et al. (2003), A large eddy simulation intercomparison study of shallow cumulus convection, *J. Atmos. Sci.*, *60*(10), 1201–1219.
Skamarock, W. C., J. B. Klemp, J. Dudhia, D. O. Gill, D. M. Barker, M. G. Duda, X.-Y. Huang, W. Wang, and J. G. Powers (2008), A description of the advanced research WRF version 3, *Tech. Rep. TN-475+STR*, National Center for Atmospheric Research, Boulder, Colo.
Sommeria, G. (1976), Three-dimensional simulation of turbulent processes in an undisturbed trade wind boundary layer, *J. Atmos. Sci.*, *33*, 216–241.
Sommeria, G., and J. W. Deardorff (1977), Subgrid-scale condensation in models of nonprecipitating clouds, *J. Atmos. Sci.*, *34*, 344–355.
Stevens, B. (2007), On the growth of layers of nonprecipitating cumulus convection, *J. Atmos. Sci.*, *64*, 2916–2931.
Stevens, B., and S. Bony (2013), What are climate models missing, *Science*, *340*(6136), 1053–1054.
Stevens, B., C. H. Moeng, and P. P. Sullivan (1999), Large-eddy simulation of radiatively driven convection: Sensitivities to the representation of small scales, *J. Atmos. Sci.*, *56*, 3963–3984.
Stevens, B., et al. (2001), Simulation of trade wind cumuli under a strong inversion, *J. Atmos. Sci.*, *58*, 1870–1891.
Stevens, B., et al. (2005), Evaluation of large-eddy simulations via observations of nocturnal marine stratocumulus, *Mon. Weather Rev.*, *133*, 1443–1462.
Stull, R. B. (1988), *An Introduction to Boundary Layer Meteorology*, Kluwer Acad., Netherlands.
Sullivan, P. P., and E. G. Patton (2011), The effect of mesh resolution on convective boundary layer statistics and structures generated by large-eddy simulation, *J. Atmos. Sci.*, *68*, 2395–2415.
Wan, H., et al. (2013), The ICON-1.2 hydrostatic atmospheric dynamical core on triangular grids—Part I: Formulation and performance of the baseline version, *Geosci. Model Dev.*, *6*, 735–763.
Willis, G. E., and J. W. Deardorff (1974), A laboratory model of the unstable planetary boundary layer, *J. Atmos. Sci.*, *31*, 1297–1307.
Wyngaard, J. C. (1985), Structure of the planetary boundary layer and implications for its modeling, *J. Appl. Meteorol. Climatol.*, *24*, 1131–1142.
Wyngaard, J. C. (2004), Toward numerical modeling in the "Terra Incognita," *J. Atmos. Sci.*, *61*, 1816–1826.
Xu, K., A. Arakawa, and S. K. Krueger (1992), The macroscopic behavior of cumulus ensembles simulated by a cumulus ensemble model, *J. Atmos. Sci.*, *49*, 2402–2420.
Xu, K.-M., and A. Arakawa (1992), Semi-prognostic tests of the Arakawa-Schubert cumulus parameterization using simulated data, *J. Atmos. Sci.*, *49*, 2421–2436.
Zängl, G., D. Reinert, M.-P. Rípodas, and M. Baldauf (2014), The ICON (icosahedral nonhydrostatic) modelling framework of DWD and MPI-M: Description of the nonhydrostatic dynamical core, *Q. J. R. Meteorol. Soc.*, *141*, 563–579, doi:10.1002/qj.2378.